ACSNANO

www.acsnano.org

ARTICLE

Mapping Orbital-Resolved Magnetism in Single Lanthanide Atoms

Aparajita Singha,[■] Daria Sostina,[■] Christoph Wolf,[■] Safa L. Ahmed, Denis Krylov, Luciano Colazzo, Pierluigi Gargiani, Stefano Agrestini, Woo-Suk Noh, Jae-Hoon Park, Marina Pivetta, Stefano Rusponi, Harald Brune, Andreas J. Heinrich, Alessandro Barla, and Fabio Donati*

Cite This: *ACS Nano* 2021, 15, 16162–16171

Read Online

ACCESS | Metrics & More | Article Recommendations | Supporting Information

ABSTRACT: **Single lanthanide atoms and molecules are promising candidates for atomic data storage and quantum logic due to the long lifetime of their magnetic quantum states. Accessing and controlling these states through electrical transport requires precise knowledge of their electronic configuration at the level of individual atomic orbitals, especially of the outer shells involved in transport. However, no experimental techniques have so far shown the required sensitivity to probe single atoms with orbital selectivity. Here we resolve the magnetism of individual orbitals in Gd and Ho single atoms on MgO/Ag(100) by combining X-ray magnetic circular dichroism with multiplet calculations and density functional theory. In contrast to the usual assumption of bulk-like occupation of the different electronic shells, we establish a charge transfer mechanism leading to an unconventional singly ionized configuration. Our work identifies the role of the valence electrons in determining the quantum level structure and spin-dependent transport properties of lanthanide-based nanomagnets.**

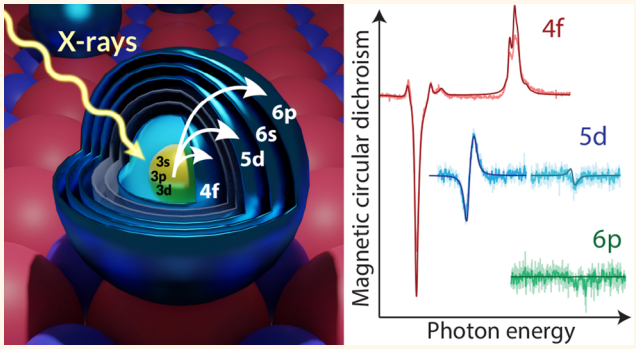

KEYWORDS: *orbital resolved magnetism, lanthanide magnetism, single atoms, X-ray magnetic circular dichroism, charge transfer*

In lanthanide elements, the spatial localization of electrons in the 4f orbitals enables strong electron correlations and gives rise to large free-atom like spin and orbital magnetic moments. When surrounded by a suitable ligand environment, lanthanide atoms can exhibit long magnetic lifetime and thereby offer an exquisite platform for information storage at the atomic scale.[1−6] In diluted samples, where magnetic interactions are negligible, one can characterize their magnetic properties using spatially averaging techniques, such as superconducting quantum interference devices[1,2,5,6] and synchrotron-based X-ray spectroscopies.[2−4] The latter not only allow probing lanthanide atoms and lanthanide-based molecules localized on supporting surfaces, but also addressing the impact of the surrounding ligand.[2−4,7] While individual access and manipulation of magnetic states of molecules was demonstrated using spin transport through electro-migrated molecular junctions,[8,9] the quantum states of individual surface-adsorbed lanthanide atoms can be sensed using spin-polarized scanning tunneling microscopy.[10−12] In these measurement schemes, the contribution of 4f electrons to spin transport is severely limited due to their strong localization. Nevertheless, access to their magnetic states is enabled through their magnetically coupled valence electrons, either localized on the molecular ligand[8,9,13] or on the outer orbitals of the atoms.[12,14] Therefore, probing the electronic configuration and spin-polarization of the valence orbitals not only allows one to design molecular magnets with multiorbital spin configuration and accessible magnetic states[15,16] but also to rationalize the quantum level structure of surface-adsorbed atoms with open valence shells.[12] However, a direct measurement of the magnetic properties of the valence electrons for surface-adsorbed isolated atoms or molecules was still missing.

Here we report measurements of valence electrons in lanthanide atoms, clusters, and films adsorbed on MgO/Ag(100) with an exquisite orbital sensitivity using X-ray absorption spectroscopy (XAS) and magnetic circular dichroism (XMCD). Conventional XAS/XMCD measurements of lanthanides generally make use of the 3d → 4f

Received: June 12, 2021
Accepted: September 15, 2021
Published: September 21, 2021

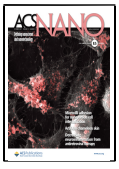

https://doi.org/10.1021/acsnano.1c05026
ACS Nano 2021, 15, 16162–16171

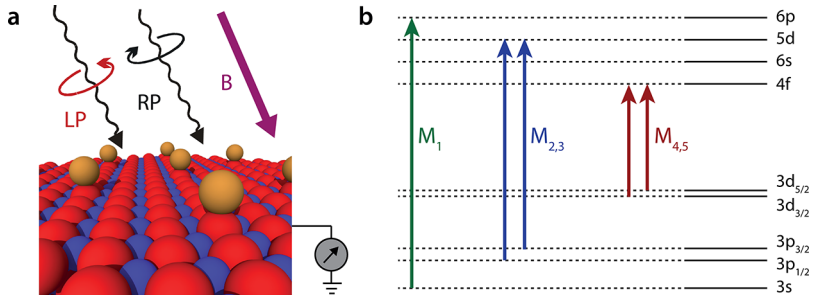

Figure 1. Orbital-selective X-ray absorption on single atoms. (a) Schematics of the XAS/XMCD measurements performed in total electron yield mode. (b) Representation of orbital sensitive measurements at M_1, $M_{2,3}$, and $M_{4,5}$ edges, which address the occupancy and magnetism of the 6p, 5d, and 4f orbitals, respectively.

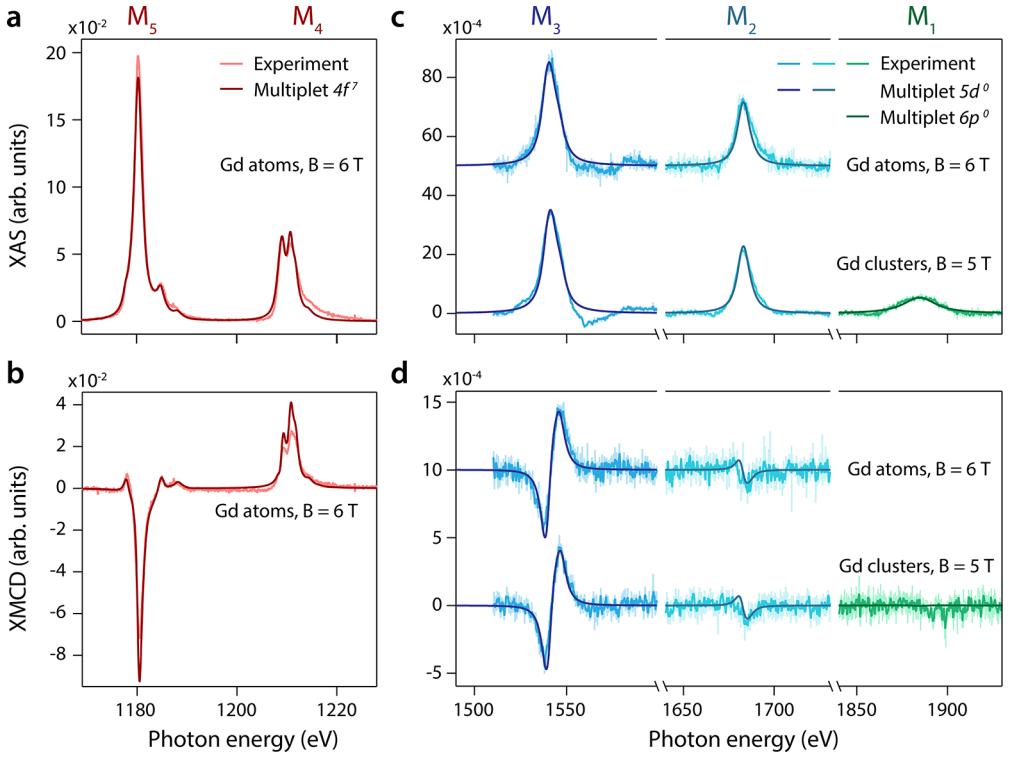

Figure 2. X-ray absorption spectra of Gd on MgO/Ag(100). (a, b) XAS and XMCD of Gd atoms (0.03 ML) at the $M_{4,5}$ edges probing the 4f orbitals. (c, d) XAS and XMCD of Gd atoms (0.03 ML) and clusters (0.14 ML) at the $M_{2,3}$ and M_1 edges probing the 5d and 6p orbitals, respectively. Raw (light solid lines) and smoothened data (solid lines) are shown together with multiplet calculations for a 4f ^{7}6s^{2}5d^{0}6p^0 configuration. Arbitrary units refer to the same intensity scale. All data were acquired in grazing incidence and represented on the same intensity scale (see the Methods).

transitions to measure the large magnetic moment of the 4f electrons. In this work, using an extended X-ray energy range, we were able to additionally access the higher energy 3p → 5d and 3s → 6p transitions to reveal the presence or absence of unpaired electrons in the 5d and 6p valence orbitals, respectively. To our knowledge, these measurements have not been reported so far for surface-adsorbed single atoms and nanostructures. To interpret our data, we developed a theoretical method combining atomic multiplet calculations with density functional theory (DFT). We first chose Gd as a test due to its stable half-filled 4f^7 configuration, weak magnetic anisotropy, and largest exchange splitting of the 5d states.[17] We then apply our method to probe the valence electrons of Ho single atoms and determine their magnetic level scheme. Ho atoms on MgO(100) thin films have attracted particular attention due to the stability of their magnetic states up to 45 K.[3,11,18−20] For both elements, we reveal an unconventional singly ionized configuration, with bulk-like occupation of the 4f shell (4f^7 for Gd, 4f^{10} for Ho), doubly occupied 6s orbitals, and no unpaired electrons in the 5d states. By mapping the spin-resolved occupation of the valence orbitals, we unravel the full-electron configuration that defines the magnetic stability of their ground state and spin-dependent transport properties.

RESULTS/DISCUSSION

The XAS and XMCD measurements were acquired using left (LP) and right (RP) circularly polarized light, as sketched in Figure 1a, in an external magnetic field **B** of up to 6 T oriented along the photon beam, while keeping the samples at low temperature (T = 6.5 K).[21] A schematic of the X-ray absorption transitions discussed in this work is presented in Figure 1b. Optical selection rules for electric dipole transitions

https://doi.org/10.1021/acsnano.1c05026
ACS Nano 2021, 15, 16162−16171

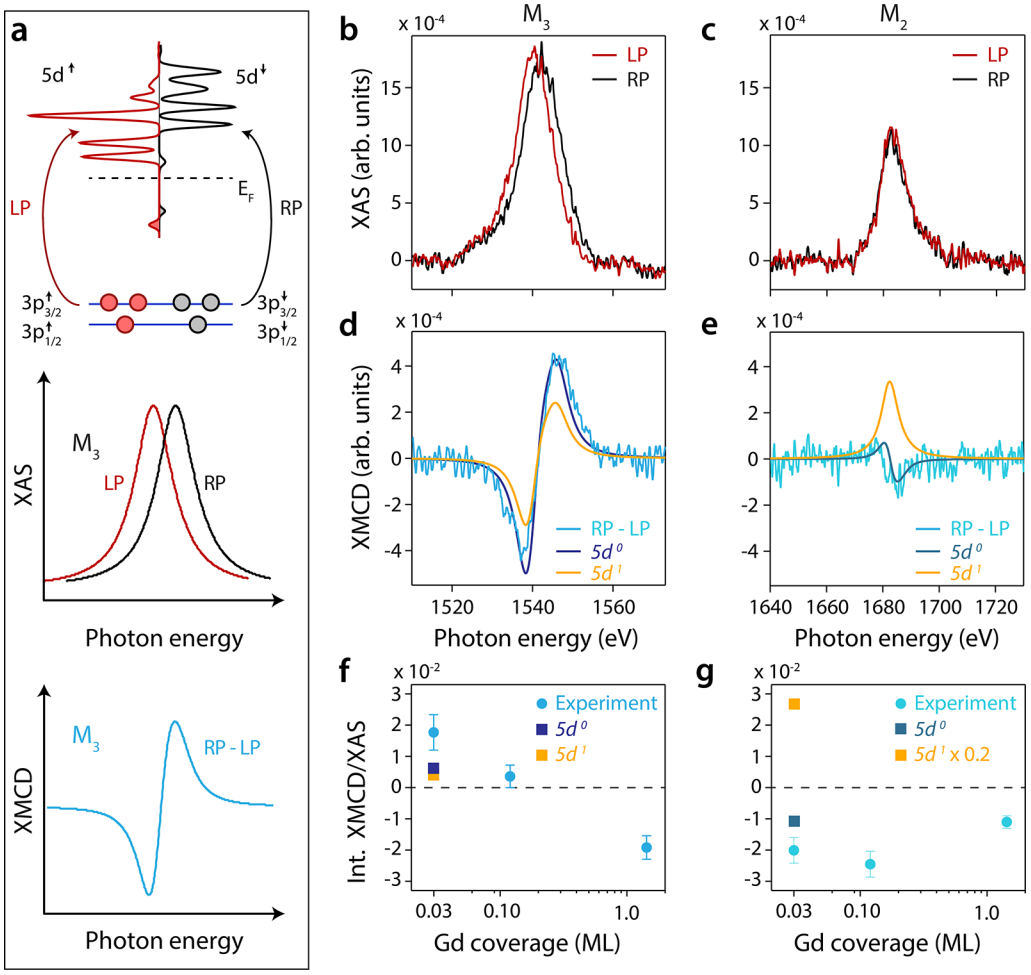

Figure 3. Analysis of the $M_{2,3}$ edges of Gd. (a) Schematics of X-ray absorption at the M_3 edge. The preferential spin-polarization generated by RP and LP photons probes the spin-split 5d states of Gd as obtained from DFT. The short lifetime of the excitation gives rise to broad peaks in the XAS. The difference of XAS signals from the two polarizations results in a derivative-like XMCD. (b, c) Polarization-resolved XAS of Gd atoms on MgO/Ag(100) at the M_3 and M_2 edges. (d, e) Corresponding XMCD signals are compared to simulations for both $5d^0$ and $5d^1$ configurations, the amplitude of which was determined by matching the experimental XAS intensity. (f, g) Integrated XMCD/XAS signals for atoms (0.03 ML), clusters (0.14 ML), and film (1.2 ML) at the M_3 and M_2 edges. All data were acquired in grazing incidence and represented on the same intensity scale (see the Methods).

impose a change of the electron angular momentum by $\Delta l = 1$ upon photon absorption. Hence, the choice of the core level determines the final state that can be probed using these transitions. Due to their larger absorption cross section, soft X-ray photons below 2000 eV are generally employed to probe the very low densities of single adatoms that are needed to ensure the absence of magnetic interactions.[22−24] In the lanthanide series, this energy range allows reaching core levels with principal quantum number $n = 3$. Therefore, only 3s → 6p (M_1), 3p → 5d ($M_{2,3}$), and 3d → 4f ($M_{4,5}$) are the allowed electric dipole transitions that can be accessed using soft X-rays, with the double subscript index labeling the spin−orbit split core states (see Figure 1b). Due to the lower cross-section, the transitions involving $\Delta l = -1$ such as 3p → 6s and 3d → 6p are much less intense and generally not considered.[25,26] While $M_{4,5}$ edges of rare earths are routinely measured in many soft X-ray beamlines, the larger energy needed to access the core levels at the M_1 and $M_{2,3}$ edges requires a specific design of the X-ray optics.[21] Here we measure the whole series of M transitions and thereby access the magnetic polarization of the individual electron shells contributing to the overall magnetization of the adatoms, especially of the outer shells contributing to electronic transport.

Figure 2 shows an overview of these measurements for Gd atoms and Gd clusters adsorbed on MgO/Ag(100) (see the Methods for sample preparation and Figure S1 for background subtraction). In this figure, we report the sum (RP + LP) of the absorption signals from the two circular polarizations as XAS and their difference (RP − LP) as XMCD. Both M_5 and M_4 peaks (Figure 2a,b) consist of a fine multiplet structure with several narrow peaks whose intensity is determined by the interactions between the open 4f and 3d shells at the excited state.[25] As shown in Figure 2b, Gd atoms exhibit a large XMCD signal on both edges, but with opposite sign. The areas under the two XMCD peaks almost compensate, which is a signature of the negligible orbital magnetic moment in this element, as expected for the case of half-filled 4f shells.[27,28] In order to ascertain the orbital configuration of Gd on MgO, we simulated the X-ray spectra using multiplet calculations including electron−electron interactions, spin−orbit coupling, the crystal field resulting from the adsorption configuration, and the external magnetic field. Besides the line width of the transitions that were chosen to match the experiment, all input

https://doi.org/10.1021/acsnano.1c05026
ACS Nano 2021, 15, 16162−16171

parameters for this model were determined *ab initio*, with only two rescaling parameters required to match the spectral shapes and relative intensities over the whole M transition series (see Methods and the Supporting Information). Both XAS and XMCD at the $M_{4,5}$ edges are well reproduced by multiplet simulations using the $4f^7$ configuration (see dark red lines). Angular and field dependent measurements of Gd 4f electrons show negligible magnetic anisotropy, which is expected for such a half-filled shell configuration with vanishing orbital moment (see Figures S2 and S3 for angle-dependent measurement of atoms and clusters).

As visible in Figure 2a,c, the intensity of the XAS signal decreases from the M_5 to the M_2 edges, and for clusters further to the M_1 edge (for single atoms, the M_1 signal is too weak to be recorded). This stems from the decreasing number of core electrons from 3d, via 3p to 3s, as well as the decreasing number of nodes in the radial matrix elements involved in 3s → 6p, 3p → 5d, and 3d → 4f transitions.[27,28] In contrast to the $M_{4,5}$ edge, the XAS line shapes of $M_{1,2,3}$ consist of a single broad peak. The absence of fine structure originates from the shorter lifetime of the final state that broadens the multiplet transitions into a single peak.[29] At the M_3, we observe a strong XMCD signal with the shape of a single peak derivative (Figure 2d). A slight dip is visible at the M_2 edge, but with reduced intensity with respect to M_3. Note that apart from the signal-to-noise ratio, the XAS and XMCD line shapes do not vary significantly from atoms to clusters and are well reproduced by our calculations using the $5d^0$ configuration. The M_1 XMCD signal of Gd clusters does not show any clear feature above our noise level, suggesting a negligible magnetic moment localized at the 6p states. Comparison with simulated spectra from multiplet calculations assuming a $6p^0$ configuration confirms this picture (Figure 2d and Figure S4).

Within the single-electron approximation, the circular polarization of the absorbed photons determines the spin-polarization of the excited photoelectrons.[28] According to the convention of magnetic field and photon axis shown in Figure 1a, LP photons at the M_3 edge excite a larger amount of spin-up electrons, while RP photons preferentially promote spin-down electrons.[30] As sketched in Figure 3a, the dichroism at this edge is hence expected to map the difference between the spin-up and spin-down 5d density of states. Due to the spin splitting of the 5d bands resulting from the intra-atomic interactions and orbital hybridization, the photon absorption produces two broad peaks centered at different energies for RP and LP. For the Gd atom data shown in Figure 2, the spectral features of the individual polarizations match well this description (see Figure 3b). Accordingly, the difference of the polarized XAS signal is expected to generate a peak derivative signal,[29] which we clearly observe at the M_3 edge of Gd/MgO, as illustrated in Figure 3d. Due to the reversed spin-polarization of the photoelectrons at the M_2 edge, the XMCD signal (Figure 3c,e) is partially reversed with respect to the M_3. These characteristic signals, so far only observed for the $L_{2,3}$ edges[30] are visible in our measurements of the $M_{2,3}$ edges of Gd adatoms, clusters and films on MgO (see Figure S5), as well as in reference samples of gadolinium(III) sulfate octahydrate (see Figure S7).

Even if the single-electron picture is sufficient for a qualitative interpretation of the XMCD line shapes, a more detailed description including multielectron configurations is required to ascertain the absence or presence of unpaired electrons in the 5d shell. For weakly hybridized systems, such as individual atoms on insulating surfaces, this approach is valid due to the close to atomic-like orbital wave functions, as will be discussed further in the text. In Figure 3d,e, we compare the results of the expected XMCD spectra for atomic $5d^0$ and $5d^1$ initial state configurations with the experiment. In order to compare the amplitudes, the sum of the two polarizations is matched to the total experimental XAS. As shown in Figure 3d, the calculated XMCD at the M_3 edge shows an almost symmetric peak derivative shape for both $5d^0$ and $5d^1$ configurations. However, only the calculated spectrum of the $5d^0$ configuration accurately matches the amplitude of the experimental XMCD signal. The inclusion of an unpaired electron impacts the simulated XMCD spectrum at the M_2 edge even more prominently. As depicted in Figure 3e, the XMCD line shape would change from being an asymmetric peak derivative expected for an initial state configuration of $5d^0$ to a positive peak-like structure for $5d^1$. Such a peak at the M_2 edge would appear due to the large orbital angular momentum and charge asymmetry expected for an unpaired electron in the localized atomic orbital. Given the absence of such a signal in our measurements, we infer the absence of unpaired electrons in the 5d shell of Gd adatoms.

Our results suggest that the electronic structure of Gd atoms adsorbed on MgO/Ag(100) is altered with respect to the free-atom ($4f^7 5d^1 6s^2 6p^0$) and to the bulk case,[31] both showing a net spin-polarization of the 5d shells. The lack of 5d polarization in surface-supported Gd atoms points toward a transfer of charge to the substrate. To validate this conjecture, we compare the XMCD of Gd atoms with that of clusters and a thin film, for which we expect to partially recover the 5d polarization of the bulk. For clusters and films, the metal bond formation distorts the atomic-like orbitals and quenches the orbital angular momentum;[32,33] hence one cannot interpret the spectral features using multiplet calculations. Therefore, in order to capture the subtle variations occurring in the XMCD spectra, we perform an analysis of the integrals of XMCD edges, which are related by the sum rules to the spin and orbital magnetic moments of the target orbitals projected along the photon-beam axis.[27,28] As shown in Figure 3f the area of the XMCD at the M_3 edge is positive for the atoms and decreases to a negative value when increasing the Gd coverage. Conversely, the area of the XMCD at the M_2 edge remains negative for all Gd coverages (Figure 3g). According to the sum rules, the absence of unpaired electrons in the ground state should naturally lead to vanishing integrals of the XMCD peaks, owing to the absence of net spin and angular momentum. Otherwise, parallel alignment of the spins to the outer magnetic field normally results in a negative value of the M_3 integral.[27,28] Hence, the trend to negative integral values at the M_3 edge indicates an increase of the spin magnetic moment and occupancy of the 5d states with increasing Gd coverage. On the other hand, the positive integral at the M_3 edge of Gd single atoms does not have a straightforward interpretation in terms of sum rules. Our multiplet calculations predict a positive value of the M_3 XMCD integral for individual Gd atoms on MgO(100), although not fully matching the experimental value. By selectively suppressing the interactions between the open shells in our calculations, we identify the origin of this effect in an indirect 4f−3p−5d coupling, which partially mixes the polarization of the 4f and 5d electrons in the final state and influences the amplitude and shape of the XMCD signal. The same effect partially explains the negative value of the integral at the M_2 edge.

https://doi.org/10.1021/acsnano.1c05026
ACS Nano 2021, 15, 16162−16171

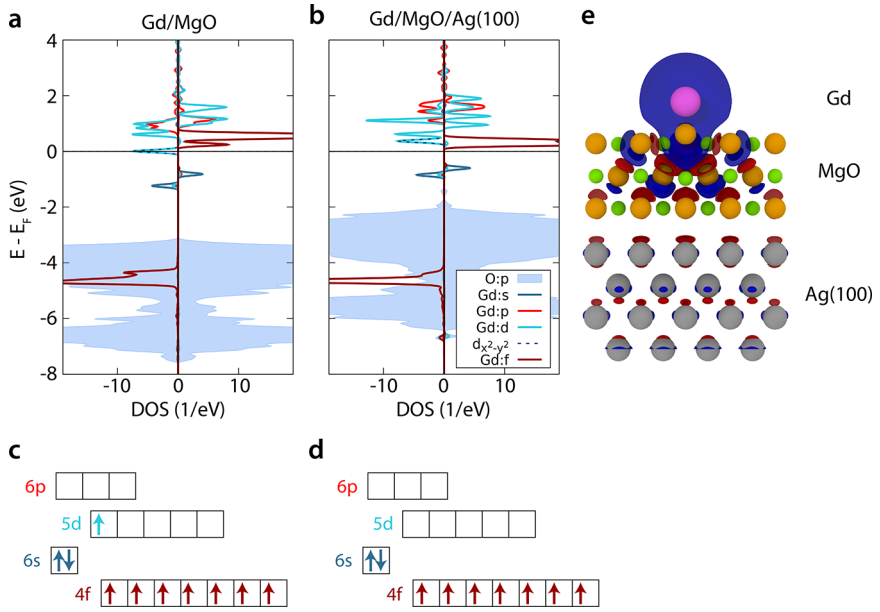

Figure 4. Density functional theory of Gd atoms on MgO/Ag(100). (a) Local spin-resolved DOS of the adatom on the oxygen-top site of 3 ML MgO and (b) of 3 ML MgO/Ag(100). (c) Schematics of the electronic configuration of Gd on MgO without and (d) with the Ag(100) substrate. (e) Cross-section along the MgO [110] direction showing the Gd/MgO/Ag(100) slab. Overplotted is the isosurface of charge density difference obtained from subtracting the electron density of the individual Gd and MgO/Ag(100) to the whole Gd/MgO/Ag(100) slab. Red/blue regions indicate positive/negative electron charge (e) variations at the isosurface of 6×10^{-4} e a_0^{-3} (a_0 being the Bohr radius). The electron charge transfer from the Gd adatom to silver can be seen as red regions around the top silver layer atoms.

Additional contribution to the XMCD integral can be ascribed to a so-called breathing effect, namely an exchange-driven contraction of the valence d shells, which introduces a spin dependence in the matrix element of the X-ray transitions.[29] This effect is particularly pronounced at the $L_{2,3}$ edges (2p → 5d transitions) of Gd bulk metal[34,35] and compounds,[31,36−38] producing a particularly strong asymmetry in the XMCD peak derivative shape. As a consequence, the XMCD integral over these edges shows a relatively large net component even for negligible occupation of the 5d orbitals, largely deviating from the values expected for atomic-like dipolar transitions.[29] This effect is particularly relevant at the $L_{2,3}$ edges due to the weak intensity of the atomic-like dipolar transitions, which are less intense than at the $M_{2,3}$ edges due to the weaker 4f−2p−5d coupling (see Figure S8). Therefore, at the $L_{2,3}$ edges the asymmetric signal of the breathing effect dominates over the weak derivative-like XMCD from atomic-like dipolar transitions. On the other hand, our results suggest that the two effects have comparable influence on the XMCD integral at the $M_{2,3}$ edges. For both $L_{2,3}$ and $M_{2,3}$ edges, the peak asymmetry introduced by the breathing effect impacts the calculations of the integrated XMCD, hence preventing a simple sum rule analysis.[37] Nevertheless, the possibility to quantify trends in the XMCD integrals extends the applicability of our approach to a wide variety of systems, from atoms with localized electrons to metal films with dispersive bands.

In order to identify the origin of the charge transfer mechanism discussed in the previous section and to understand the individual roles of the MgO film and supporting Ag(100) substrate, we performed density functional theory (DFT) calculations of the Gd atoms adsorbed on the oxygen-top site of both bare MgO(100) and MgO/Ag(100),[3,39,40] in both cases using a MgO thickness of 3 monolayers (ML). We found that Gd adsorbs approximately 2.71 Å above the top layer of MgO and the underlying oxygen is displaced toward the Gd resulting in a Gd−O bond length of 2.15 Å, as illustrated in Figure 4e. This lattice distortion is very similar to what was found for Ho/MgO in former DFT calculations.[3,39] To gain insight into the resulting electronic structure, we calculated the projected density of states (PDOS) for both Gd/MgO (Figure 4a) and Gd/MgO/Ag(100) (Figure 4b). For both cases, the related Löwdin charge analysis (Table 1) finds seven electrons in the 4f shell, in agreement with the experiment. The PDOS plots reveal full polarization of these states, with the majority 4f electrons giving rise to a large localized magnetic moment. In addition, both calculations reveal equally occupied 6s majority and minority orbitals lying below the Fermi level, with resulting negligible net polarization (Figure 4a,b). The 6p orbitals are essentially empty and positioned at about 2 eV above the Fermi level.

Table 1. DFT Calculated Effective Charges for Gd Free-Atom, Gd Adsorbed on Bare MgO, and Gd on MgO/Ag(100) Calculated with the Löwdin Scheme[a]

orbital	free atom	Gd/MgO	Gd/MgO/Ag(100)	charge difference
6s	2.0 (0.0)	1.06 (0.01)	1.10 (0.02)	0.04
6p	0.0 (0.0)	0.24 (0.05)	0.23 (0.00)	−0.01
5d	1.0 (1.0)	1.54 (1.04)	0.71 (0.08)	−0.83
4f	7.0 (7.0)	7.16 (6.99)	7.16 (6.93)	0.00
total	10.0 (8.0)	10.00 (8.09)	9.20 (7.03)	**−0.80**

[a]The charge difference due to the presence of the Ag substrate is given in the last column. All values are provided in electron charges. For the 6s and 6p orbitals, the charges have been obtained by subtracting 2 and 6 electrons from the total charge obtained for the 5s + 6s and 5p + 6p, respectively, as obtained from the Löwdin analysis. Values in brackets represent the spin-polarization of each orbital.

https://doi.org/10.1021/acsnano.1c05026
ACS Nano 2021, 15, 16162−16171

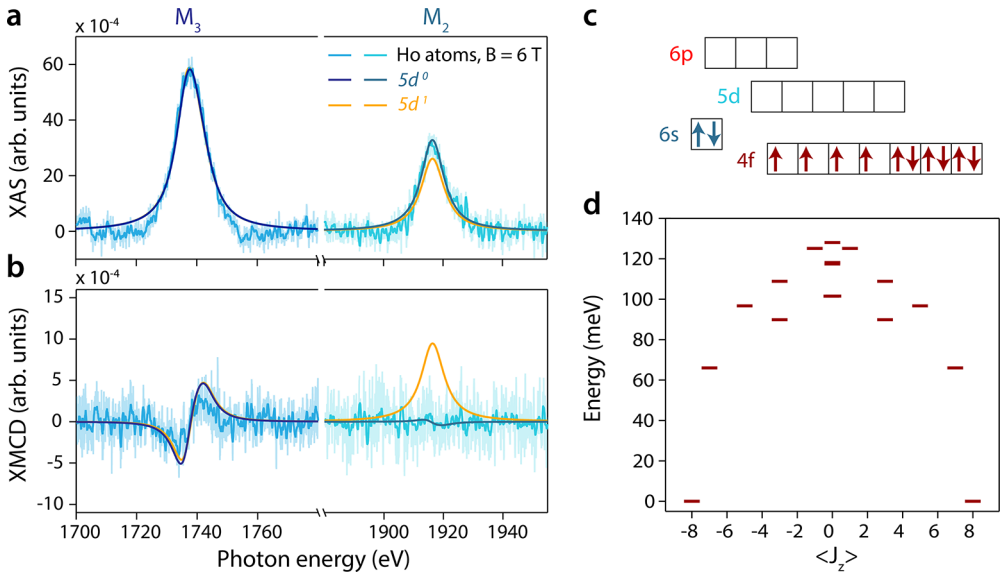

Figure 5. XAS and XMCD of Ho atoms on MgO/Ag(100). (a) XAS and (b) XMCD spectra for Ho atoms (0.03 ML) at the $M_{2,3}$ edges. Raw (light solid lines) and smoothened data (solid lines) are shown together with multiplet calculations for $5d^0$ and $5d^1$ configurations, the amplitude of which was determined by matching the experimental XAS intensity. (c) Orbital occupation of Ho atoms inferred from the analysis of the $M_{2,3}$ edges. The lowest energy multiplet is characterized by S = 2, L = 6, and J = 8 quantum numbers. (d) Splitting of the magnetic states from the lowest multiplet due to the crystal field, revealing a ground state with $J_z \approx \pm 8$. To maximize the magnetic signal in the presence of the Ho out-of-plane anisotropy,[3] all data were acquired in normal incidence (see the Methods).

On the other hand, the total Gd charge, as well as the occupation of the 5d orbitals, are strongly affected by the Ag(100) substrate. For Gd on MgO(100), we find the total charge state to be identical to the free neutral atom. Differently from the free atom, we find an electronic redistribution occurring mostly between the 6s and $5d_{z^2}$, which results from the on-site hybridization upon adsorption at the MgO surface. However, the total polarization of the outer shells is not altered, leaving essentially one unpaired electron in the 5d shell as sketched in panel Figure 4c. Conversely, when the silver substrate is included, we find an effective charge transfer of 0.80 electrons to the substrate, which essentially coincides with the variations occurring in the Gd 5d orbital (−0.83 electrons). The main variation in the electron states occurs in the planar $5d_{x^2-y^2}$ orbital, which is the lowest in energy in the MgO crystal field (see Figures S9 and S10). Due to this charge rearrangement, the 5d states become essentially nonpolarized (Figure 4b,d), in agreement with our measurements. In both scenarios, the strong atomic-like character of this state justifies the interpretation of the XMCD spectra of Gd atoms on MgO/Ag(100) using multiplet calculations. The charge is mostly transferred from the lanthanide to the states localized at the MgO/Ag(100) interface (Figure 4e). Such an effect has been quite commonly observed to occur in ultrathin oxide layers on metal surfaces[41] as well as on metal-supported graphene layers.[12] Due to this charge transfer, the atom is left in a formal "Gd^{1+}" charge state. Note that, differently from the $5d^0$ configuration inferred from the multiplet analysis, DFT finds a residual charge of 0.7 electrons in the 5d orbitals even in the presence of Ag(100). This value is mostly a result of the hybridization between Gd and MgO states. The difference between the two analyses originates from the absence of covalence in the multiplet approach that prevents an accurate modeling of the ligand charges. However, since this fraction of 5d electrons has only negligible spin-polarization, it does not provide a significant contribution to the XMCD signal. In addition, no strongly polarized state is localized at the Fermi level, with the lowest majority 5d states available at around +200 meV. The absence of polarized valence electrons is expected to result in a small magnetic signal in transport measurements.

We now apply the understanding gathered from the orbital-sensitive M-edge measurements of Gd atoms and clusters on MgO to explore the orbital occupation and magnetism of Ho single atom magnets. Similar to Gd atoms, the signal at the Ho M_1 edge was too weak to be detected for samples with well-separated single atoms. All input parameters for the multiplet calculations of Ho have been taken either from our *ab-initio* calculations or from a previous report in the literature,[42] leaving no free parameters to the model except for the line width of the transitions (see the Methods and the Supporting Information). The normalized XAS and XMCD at the $M_{4,5}$ edges (see Figure S11) indicate $4f^{10}$ occupancy for Ho atoms, in agreement with earlier work.[3] The measurements of the $M_{2,3}$ edge show similar behavior to what we have observed for Gd, i.e., derivative-like XMCD at the M_3 edge and the absence of a peak structure at the M_2 edge (Figure 5a,b). The magnitude of the XMCD at both edges is, however, quite reduced with respect to Gd. This effect is due to the smaller number of unpaired electrons at the 4f orbitals that induce a smaller exchange splitting of the 5d bands.[17] The reduced intensity of the XMCD at these edges is well matched by our multiplet calculations. For the case of Ho atoms, the intensity and shape of the XMCD at the M_3 edge is well matched by both $5d^1$ and $5d^0$ calculations, preventing a clear distinction between the presence or absence of an unpaired electron in the 5d states. On the other hand, the negligible XMCD at the M_2 edge is at odd with the peak shape and amplitude predicted for $5d^1$ configuration, while it agrees well with the intensity expected in case of no unpaired electrons in the 5d orbitals.

Recent calculations of Ho on MgO(100)[43] found very similar electronic structures to that of Gd on MgO shown in

https://doi.org/10.1021/acsnano.1c05026
ACS Nano 2021, 15, 16162−16171

this paper. In the absence of the Ag(100) substrate, DFT finds Ho in a $6s^2 6p^0$ configuration, with an additional unpaired electron in an atomic-like $5d_{x^2-y^2}$ orbital. In contrast, our measurements indicate that this orbital is depleted and validate the idea of a charge transfer to the Ag(100) substrate, as observed for Gd. The resulting electronic configuration of Ho atoms on MgO/Ag(100) is summarized in Figure 5c. In this electronic configuration, multiplet calculations predict a ground state multiplet with maximum spin $\mathbf{S} = 2$, orbital $\mathbf{L} = 6$, and total angular momentum $\mathbf{J} = 8$, as also expected by Hund's rules. The crystal field provided by the MgO splits the 17 states of this multiplet, as shown in Figure 5d. In the absence of singly occupied 5d electrons, the main contribution to the splitting comes from the proximity of the oxygen ion underneath the Ho, which generates a large uniaxial anisotropy and favors a ground state doublet with maximum projection $\mathbf{J}_z \approx \pm 8$ along the out-of-plane direction. For such a ground state, we find a total magnetic moment of 9.9 μB, which agrees with previous STM results.[10,11] Hence, our findings eliminate one of the two quantum level configurations proposed so far,[11] which required the presence of an unpaired electron in the valence orbitals to explain the total magnetic moment of Ho atoms.

The perturbation of the neighboring Mg and O ions further splits originally conjugated doublets into pairs of singlet states with $\mathbf{J}_z \approx \pm 0$ at the top of the barrier. As discussed in previous works, these states can offer effective pathways to reverse the magnetization of the atom using high-energy electrons.[10,11] Nevertheless, our calculations show that the ground state doublet preserves a very strong axial character; i.e., its value of $\mathbf{J}_z$ is very close to the maximum theoretical value. Although such a ground state is not considered magnetically stable in the 4-fold symmetric ligand field of the oxygen-top adsorption site, the strong uniaxial component of the crystal field dominates over the transverse perturbative terms. In this configuration, a weak but detectable quantum tunneling can limit the stability of the system at very low fields, as also found in a previous work.[20]

As discussed for Gd, the absence of polarized 5d electrons is expected to result in a very small magnetic contribution to the conductance in transport measurements. Previous spin-polarized STM results on Ho atoms on MgO/Ag(100) found a rather low magnetic contrast of about 4% of the total conductance.[10,11,20,44] This value is an order of magnitude smaller than for Fe on the same substrate[45] and for Dy atoms on graphene/Ir(111), for which an unpaired electron in the 6s orbitals provides a large magnetic contribution to the tunneling conductance.[12]

CONCLUSIONS

In summary, our XMCD measurements, combined with density functional theory and crystal-field based multiplet analysis, corroborate a bulk-like $4f^n$ configuration for both Gd and Ho ($n = 7$ for Gd, $n = 10$ for Ho). For neutral species, this implies a singly occupied 5d orbital. However, we find no evidence of unpaired electrons in the valence shell of these late lanthanides. The absence of polarization of the 5d states is ascribed to an effective charge transfer of almost one electron from the rare earth adatoms to the Ag(100) substrate. This singly ionized state is quite unconventional in rare earth elements, which are mostly found in neutral, divalent, or trivalent states.[46] The key to obtain this unconventional configuration is the presence of an ionic support that offers a single uniaxial bond to the adatom, with limited possibility of orbital hybridization and charge transfer. In this situation, charge transfer can only occur due to the proximity of the underlying metal substrate. Consequently, the rare earth electron tunnels through the MgO film and reaches the empty states of Ag(100). The resulting low polarization of the outer shells explains previous STM results showing low magnetic contrast on lanthanide atoms on MgO/Ag(100).[10,11,20,44]

The orbital selectivity demonstrated in this work allows us to address charge transfer effects and to map full-electronic configurations, which crucially impact the structure of quantum levels of nanostructures on surfaces, such as few-atom clusters[47,48] and single molecule magnets.[15,16,49,50] Thereby our study outlines a strategy to design lanthanide-based atomic-scale systems with highly localized states utilizing exchange-coupled valence orbitals as a read-out channel in electrical transport measurements.

METHODS

Sample Preparation. Single crystals of Ag(100) were prepared by repeated cycles of sputtering and subsequent annealing at 773 K. Films of MgO with thicknesses between 3 and 6 monolayers (MLs) were grown by thermal evaporation of Mg in O_2 partial pressure of 1×10^{-6} mbar, with the substrate kept at 623 K and a Mg flux yielding a growth rate of about 0.2 ML/min. One monolayer is defined as one MgO(100) unit cell per Ag(100) substrate atom. The calibration of the MgO thickness was obtained by measuring the Mg XAS K edge and comparing to previous works.[3,7,51] The MgO/Ag(100) samples were transferred to the measurement position without breaking the vacuum. Gadolinium and holmium atoms were deposited from thoroughly degassed rods or lumps (purity 99%) from W crucibles, directly onto the substrate held at less than 10 K, in order to prevent surface diffusion, and in a base pressure of 1×10^{-10} mbar.[3,40] Also for the adsorbed elements, we define 1 ML as one lanthanide atom per Ag(100) substrate atom and calibrated the amount by comparison with former experiments.[3,18] In the absence of a detailed study of the growth mode of rare earth atoms and clusters on MgO/Ag(100), the amount of atoms in the ensemble is estimated by comparison with previous studies of Er on Cu(111)[47] and of Dy on graphene/Ir(111).[52,53] Due to the very different lattice constant of these substrates, it is more appropriate to compare the amount of lanthanide atoms in terms of absolute surface density instead of surface atomic coverage. Former studies show that the large majority of Ho atoms (up to 93%) adsorb on top of oxygen on 2 or more MgO layers on Ag(100).[3,39,40] Similar behavior was also observed for other lanthanide atoms.[40] For adsorption on top of oxygen, 0.03 ML of Gd and Ho atoms corresponds to 0.354 atoms/nm^2. On Cu(111) and graphene/Ir(111), the same surface density corresponds to a coverage of 0.02 ML, for which the statistical abundance of atoms is 93% and 74%, respectively. Therefore, for samples with 0.03 ML of Gd or Ho, the XAS/XMCD signals are representative of individual uncorrelated atoms adsorbed on top of oxygen atoms. In addition, at this coverage we expect the magnetic interactions between atoms to be extremely low. Former XMCD studies on Co/Pt(111) at 5 K reveal no detectable magnetic coupling from 0.003 to 0.03 ML. These interactions are found to be even weaker for lanthanide atoms on insulators, for which dipolar coupling represents the only relevant interaction and show a characteristic energy scale that is much smaller than the thermal energy of our experiment.[10] Hence, we can safely exclude magnetic interactions to play a role in determining the properties of ensembles of atoms at the lowest coverage used in our experiment.

XAS and XMCD Measurements. The XAS and XMCD spectra shown in the main text were acquired at the BOREAS beamline of the ALBA synchrotron,[21] with additional measurements done at the EPFL/PSI X-Treme beamline at the Swiss Light Source,[54] and at the 6A MeXiM beamline at Pohang Light Source-II. The XAS/XMCD acquisitions were performed with circularly polarized light in the total

https://doi.org/10.1021/acsnano.1c05026
ACS Nano 2021, 15, 16162−16171

electron yield (TEY) mode at sample temperatures of T = 6.5 K (BOREAS), T = 2.5 K (X-Treme), or T = 15 K (MeXiM), and in external magnetic fields up to **B** = 6.8 T parallel to the X-ray beam. In TEY mode, the photoionized atoms at the surface are neutralized by an external electrical current, whose intensity is proportional to the photon absorption. The TEY is obtained as the ratio between the intensity of the sample current and the intensity of the X-ray beam (photoionizing current from a gold mesh placed upstream on the beamline). We observe no transient effects during the signal acquisition, indicating negligible charging occurring at the sample surface. Two different incidence geometries have been used to explore the angular dependence of the magnetic moments (see Figures S2 and S3), namely normal incidence, with both the beam and the field perpendicular to the surface, and grazing incidence, with the sample rotated by 60° with respect to the beam and field direction.

XAS and XMCD Data Analysis. In order to isolate the contribution of the lanthanide atoms and clusters from the background signal, spectra of bare MgO/Ag(100) over the lanthanide edges were recorded prior to Gd or Ho deposition and subtracted from the final spectra (see Figure S1). The spectra at different edges of the atoms have been normalized to the value of the integrated XAS at the $M_{4,5}$ edges. In order to compare the $M_{2,3}$ edges of atoms, clusters, and films, the values have been normalized to the summed XAS over these two edges.

DFT Calculations. DFT calculations were performed using plane-wave basis and pseudopotentials as implemented in Quantum Espresso with pseudopotentials from the SSSP library.[55,56] All pseudopotentials use the generalized gradient approximation for the exchange−correlation potential. The sample was modeled as 4 ML of silver fixed at the lattice constant of bulk silver (a_{Ag} = 4.16 Å) capped by 3 ML of MgO and the adatom which is laterally separated from its period images by more than 12 Å. The cell is padded by 15 Å of vacuum to decouple the slab from its periodic image in the z-direction. Integration of the Brillouin zone used a 5 × 5 × 1 Monkhorst−Pack grid[57] and a cutoff of 50 and 500 Ry was used for the plane wave expansion and the charge density, respectively. We performed a relaxation of the system until the residual forces were less than 10^{-3} Ry/a_0 (a_0 is the Bohr radius). To corroborate our finding of charge transfer from the adatom to the underlying Ag substrate, we performed additional calculations after removing the silver. This can be interpreted as the limiting case of very thick MgO films. The structure was not further relaxed, and all other parameters are identical to the calculations that include the silver layer.

Atomic Multiplet Simulations. Simulated X-ray spectra were computed using the Quanty multielectron code.[58] Open shell multiplet calculations of the Gd and Ho atoms were performed by modeling the intra- and inter-orbital interactions using Slater integrals, whose values were obtained from full-electron Cowan's atomic structure code.[59] For both Gd and Ho, all Slater integrals were calculated assuming doubly occupied 6s orbitals, $4f^n$ configuration with n = 7 for Gd and n = 10 for Ho. The values were rescaled to account for the screening provided by surface electrons. Rescaled values are provided in Table S2. Simulations of both empty and singly occupied 5d and 6p orbitals were performed as indicated in the text. In addition to electron−electron interactions, the Hamiltonian for the multiplet calculations also includes spin−orbit coupling, Zeeman energy due to the external magnetic field and crystal field acting on the different shells. Spin−orbit values were computed using Cowan's atomic structure code. The final state Hamiltonian includes the presence of the core hole and additional valence electron according to the simulated transitions. The crystal field acting on the open shells of lanthanide was modeled according to the nature of the open valence shell. For delocalized 5d and 6p electrons, the splitting of the orbitals was obtained from DFT by means of Wannier functions method (see Supporting Information). This method is, however, not accurate enough to be applied to the highly localized and correlated 4f electrons. In this case, we modeled the crystal field acting on the 4f orbitals using a point charge electrostatic model[60,61] including only the nearest neighbors of the adsorbed lanthanide. The position and charge values of the neighboring ions around the Gd and Ho atoms obtained from DFT are provided in Table S3. The value of the crystal field parameters used for the calculations are summarized in Tables S4, S5, and S6. The XAS and XMCD spectra were calculated using the Green's function method.[58]

ASSOCIATED CONTENT

Supporting Information

The Supporting Information is available free of charge at https://pubs.acs.org/doi/10.1021/acsnano.1c05026.

Details on the XAS and XMCD measurements; data analysis; multiplet and DFT calculations; XAS and XMCD spectra, PDOS plots, and density images; tables of splitting parameters, rescaling parameters, charges and positions, and crystal field parameters, (PDF)

AUTHOR INFORMATION

Corresponding Author

Fabio Donati − *Center for Quantum Nanoscience, Institute for Basic Science (IBS), Seoul 03760, Republic of Korea; Department of Physics, Ewha Womans University, Seoul 03760, Republic of Korea;* orcid.org/0000-0002-3932-2889; Email: donati.fabio@qns.science

Authors

Aparajita Singha − *Center for Quantum Nanoscience, Institute for Basic Science (IBS), Seoul 03760, Republic of Korea; Ewha Womans University, Seoul 03760, Republic of Korea; Max Planck Institute for Solid State Research, Stuttgart 70569, Germany;* orcid.org/0000-0001-6301-0394

Daria Sostina − *Center for Quantum Nanoscience, Institute for Basic Science (IBS), Seoul 03760, Republic of Korea; Ewha Womans University, Seoul 03760, Republic of Korea*

Christoph Wolf − *Center for Quantum Nanoscience, Institute for Basic Science (IBS), Seoul 03760, Republic of Korea; Ewha Womans University, Seoul 03760, Republic of Korea;* orcid.org/0000-0002-9340-9782

Safa L. Ahmed − *Center for Quantum Nanoscience, Institute for Basic Science (IBS), Seoul 03760, Republic of Korea; Department of Physics, Ewha Womans University, Seoul 03760, Republic of Korea*

Denis Krylov − *Center for Quantum Nanoscience, Institute for Basic Science (IBS), Seoul 03760, Republic of Korea; Ewha Womans University, Seoul 03760, Republic of Korea*

Luciano Colazzo − *Center for Quantum Nanoscience, Institute for Basic Science (IBS), Seoul 03760, Republic of Korea; Ewha Womans University, Seoul 03760, Republic of Korea*

Pierluigi Gargiani − *ALBA Synchrotron Light Source, 08290 Catalonia, Spain;* orcid.org/0000-0002-6649-0538

Stefano Agrestini − *ALBA Synchrotron Light Source, 08290 Catalonia, Spain;* orcid.org/0000-0002-3625-880X

Woo-Suk Noh − *MPPC−CPM, Max Planck POSTECH, Pohang 37673, Republic of Korea*

Jae-Hoon Park − *Department of Physics, Pohang University of Science and Technology (POSTECH), Pohang 37673, Republic of Korea*

Marina Pivetta − *Institute of Physics, École Polytechnique Fédérale de Lausanne, CH-1015 Lausanne, Switzerland;* orcid.org/0000-0001-5330-8648

Stefano Rusponi − *Institute of Physics, École Polytechnique Fédérale de Lausanne, CH-1015 Lausanne, Switzerland;* orcid.org/0000-0002-8494-5532

Harald Brune − *Institute of Physics, École Polytechnique Fédérale de Lausanne, CH-1015 Lausanne, Switzerland;* orcid.org/0000-0003-4459-3111

Andreas J. Heinrich − *Center for Quantum Nanoscience, Institute for Basic Science (IBS), Seoul 03760, Republic of Korea; Department of Physics, Ewha Womans University, Seoul 03760, Republic of Korea;* orcid.org/0000-0001-6204-471X

Alessandro Barla − *Istituto di Struttura della Materia (ISM), Consiglio Nazionale delle Ricerche (CNR), I-34149 Trieste, Italy*

Complete contact information is available at: https://pubs.acs.org/10.1021/acsnano.1c05026

Author Contributions

A.S., D.S., S.L.A., D.K., L.C., P.G., W.S.N., M.P, S.R., A.B., and F.D. performed the XAS/XMCD synchrotron experiments. The analysis of the XAS/XMCD data using multiplet calculations have been performed by A.S., D.S., S.A., and F.D. DFT calculations have been performed by C.W. J.H.P., H.B., and A.J.H. secured funding. The manuscript was written through contributions of all authors. All authors have given approval to the final version of the manuscript.

Author Contributions

■A.S., D.S., and C.W. contributed equally.

Funding

Institute of Basic Science, Korea; National Research Foundation of Korea (NRF).

Notes

The authors declare no competing financial interest.

ACKNOWLEDGMENTS

A.S., D.S., C.W., S.L.A., D.K., L.C., A.J.H., and F.D. acknowledges funding from the Institute of Basic Science, Korea, through the Project No. IBS319 R027-D1. W.S.N. and J.H.P. acknowledge funding from the National Research Foundation of Korea (NRF) funded by the Ministry of Science and ICT (No. 2016K1A4A4A01922028). The authors acknowledge Mariia Krylova for her assistance with the TOC figure.

REFERENCES

(1) Ishikawa, N.; Sugita, M.; Ishikawa, T.; Koshihara, S.; Kaizu, Y. Lanthanide Double-Decker Complexes Functioning as Magnets at the Single-Molecular Level. *J. Am. Chem. Soc.* **2003**, *125*, 8694−8695.

(2) Westerstrom, R.; Dreiser, J.; Piamonteze, C.; Muntwiler, M.; Weyeneth, S.; Brune, H.; Rusponi, S.; Nolting, F.; Popov, A.; Yang, S.; Dunsch, L.; Greber, T. An Endohedral Single-Molecule Magnet with Long Relaxation Times: Dysc2n@C80. *J. Am. Chem. Soc.* **2012**, *134*, 9840−9843.

(3) Donati, F.; Rusponi, S.; Stepanow, S.; Wäckerlin, C.; Singha, A.; Persichetti, L.; Baltic, R.; Diller, K.; Patthey, F.; Fernandes, E.; Dreiser, J.; Sljivancanin, Z.; Kummer, K.; Nistor, C.; Gambardella, P.; Brune, H. Magnetic Remanence in Single Atoms. *Science* **2016**, *352*, 318−321.

(4) Baltic, R.; Pivetta, M.; Donati, F.; Wäckerlin, C.; Singha, A.; Dreiser, J.; Rusponi, S.; Brune, H. Superlattice of Single Atom Magnets on Graphene. *Nano Lett.* **2016**, *16*, 7610−7615.

(5) Goodwin, C. A. P.; Ortu, F.; Reta, D.; Chilton, N. F.; Mills, D. P. Molecular Magnetic Hysteresis at 60 K in Dysprosocenium. *Nature* **2017**, *548*, 439−442.

(6) Guo, F. S.; Day, B. M.; Chen, Y. C.; Tong, M. L.; Mansikkamaki, A.; Layfield, R. A. Magnetic Hysteresis up to 80 K in a Dysprosium Metallocene Single-Molecule Magnet. *Science* **2018**, *362*, 1400−1403.

(7) Wäckerlin, C.; Donati, F.; Singha, A.; Baltic, R.; Rusponi, S.; Diller, K.; Patthey, F.; Pivetta, M.; Lan, Y.; Klyatskaya, S.; Ruben, M.; Brune, H.; Dreiser, J. Giant Hysteresis of Single-Molecule Magnets Adsorbed on a Nonmagnetic Insulator. *Adv. Mater.* **2016**, *28*, 5195−5199.

(8) Vincent, R.; Klyatskaya, S.; Ruben, M.; Wernsdorfer, W.; Balestro, F. Electronic Read-Out of a Single Nuclear Spin Using a Molecular Spin Transistor. *Nature* **2012**, *488*, 357−360.

(9) Thiele, S.; Balestro, F.; Ballou, R.; Klyatskaya, S.; Ruben, M.; Wernsdorfer, W. Electrically Driven Nuclear Spin Resonance in Single-Molecule Magnets. *Science* **2014**, *344*, 1135−1138.

(10) Natterer, F. D.; Yang, K.; Paul, W.; Willke, P.; Choi, T.; Greber, T.; Heinrich, A. J.; Lutz, C. P. Reading and Writing Single-Atom Magnets. *Nature* **2017**, *543*, 226−228.

(11) Natterer, F. D.; Donati, F.; Patthey, F.; Brune, H. Thermal and Magnetic-Field Stability of Holmium Single-Atom Magnets. *Phys. Rev. Lett.* **2018**, *121*, 027201.

(12) Pivetta, M.; Patthey, F.; Di Marco, I.; Subramonian, A.; Eriksson, O.; Rusponi, S.; Brune, H. Measuring the Intra-Atomic Exchange Energy in Rare-Earth Adatoms. *Phys. Rev. X* **2020**, *10*, 031054.

(13) Komeda, T.; Isshiki, H.; Liu, J.; Zhang, Y.-F.; Lorente, N.; Katoh, K.; Breedlove, B. K.; Yamashita, M. Observation and Electric Current Control of a Local Spin in a Single-Molecule Magnet. *Nat. Commun.* **2011**, *2*, 217.

(14) Coffey, D.; Diez-Ferrer, J. L.; Serrate, D.; Ciria, M.; de la Fuente, C.; Arnaudas, J. I. Antiferromagnetic Spin Coupling between Rare Earth Adatoms and Iron Islands Probed by Spin-Polarized Tunneling. *Sci. Rep.* **2015**, *5*, 13709.

(15) Meihaus, K. R.; Fieser, M. E.; Corbey, J. F.; Evans, W. J.; Long, J. R. Record High Single-Ion Magnetic Moments through $4f^n5d^1$ Electron Configurations in the Divalent Lanthanide Complexes $[(C_5h_4sime_3)_3ln]^-$. *J. Am. Chem. Soc.* **2015**, *137*, 9855−9860.

(16) Gould, C. A.; McClain, K. R.; Yu, J. M.; Groshens, T. J.; Furche, F.; Harvey, B. G.; Long, J. R. Synthesis and Magnetism of Neutral, Linear Metallocene Complexes of Terbium(Ii) and Dysprosium(Ii). *J. Am. Chem. Soc.* **2019**, *141*, 12967−12973.

(17) Brown, S. D.; Strange, P.; Bouchenoire, L.; Zarychta, B.; Thompson, P. B. J.; Mannix, D.; Stockton, S. J.; Horne, M.; Arola, E.; Ebert, H.; Szotek, Z.; Temmerman, W. M.; Fort, D. Dipolar Excitations at the L_{iii} X-Ray Absorption Edges of the Heavy Rare-Earth Metals. *Phys. Rev. Lett.* **2007**, *99*, 247401.

(18) Donati, F.; Rusponi, S.; Stepanow, S.; Persichetti, L.; Singha, A.; Juraschek, D. M.; Wäckerlin, C.; Baltic, R.; Pivetta, M.; Diller, K.; Nistor, C.; Dreiser, J.; Kummer, K.; Velez-Fort, E.; Spaldin, N. A.; Brune, H.; Gambardella, P. Unconventional Spin Relaxation Involving Localized Vibrational Modes in Ho Single-Atom Magnets. *Phys. Rev. Lett.* **2020**, *124*, 077204.

(19) Donati, F. Magnetic Relaxation Mechanisms in Ho Single Atom Magnets. *J. Magn.* **2020**, *25*, 441−452.

(20) Forrester, P. R.; Patthey, F.; Fernandes, E.; Sblendorio, D. P.; Brune, H.; Natterer, F. D. Quantum State Manipulation of Single Atom Magnets Using the Hyperfine Interaction. *Phys. Rev. B: Condens. Matter Mater. Phys.* **2019**, *100*, 180405.

(21) Barla, A.; Nicolás, J.; Cocco, D.; Valvidares, S. M.; Herrero-Martín, J.; Gargiani, P.; Moldes, J.; Ruget, C.; Pellegrin, E.; Ferrer, S. Design and Performance of Boreas, the Beamline for Resonant X-Ray Absorption and Scattering Experiments at the Alba Synchrotron Light Source. *J. Synchrotron Radiat.* **2016**, *23*, 1507−1517.

(22) Gambardella, P.; Dhesi, S. S.; Gardonio, S.; Grazioli, C.; Ohresser, P.; Carbone, C. Localized Magnetic States of Fe, Co, and Ni Impurities on Alkali Metal Films. *Phys. Rev. Lett.* **2002**, *88*, 047202.

(23) Nistor, C.; Mugarza, A.; Stepanow, S.; Gambardella, P.; Kummer, K.; Diez-Ferrer, J. L.; Coffey, D.; de la Fuente, C.; Ciria, M.; Arnaudas, J. I. Structure and Magnetism of Tm Atoms and Monolayers on W(110). *Phys. Rev. B: Condens. Matter Mater. Phys.* **2014**, *90*, 064423.

(24) Donati, F.; Singha, A.; Stepanow, S.; Wäckerlin, C.; Dreiser, J.; Gambardella, P.; Rusponi, S.; Brune, H. Magnetism of Ho and Er

Atoms on Close-Packed Metal Surfaces. *Phys. Rev. Lett.* **2014**, *113*, 237201.
(25) Thole, B. T.; van der Laan, G.; Fuggle, J. C.; Sawatzky, G. A.; Karnatak, R. C.; Esteva, J. 3d X-Ray-Absorption Lines and the $3d^94f^{n+1}$ Multiplets of the Lanthanides. *Phys. Rev. B: Condens. Matter Mater. Phys.* **1985**, *32*, 5107−5118.
(26) Kiyono, S.; Chiba, S.; Hayasi, Y.; Kato, S.-i.; Mochimaru, S. Extended Absorption Fine Structure in the Soft X-Ray Region. *Jpn. J. Appl. Phys.* **1978**, *17*, 212.
(27) Thole, B. T.; Carra, P.; Sette, F.; van der Laan, G. X-Ray Circular Dichroism as a Probe of Orbital Magnetization. *Phys. Rev. Lett.* **1992**, *68*, 1943−1946.
(28) Carra, P.; Thole, B. T.; Altarelli, M.; Wang, X. X-Ray Circular Dichroism and Local Magnetic Fields. *Phys. Rev. Lett.* **1993**, *70*, 694−697.
(29) van Veenendaal, M.; Goedkoop, J. B.; Thole, B. T. Branching Ratios of the Circular Dichroism at Rare Earth L_{23} Edges. *Phys. Rev. Lett.* **1997**, *78*, 1162−1165.
(30) Parlebas, J. C.; Asakura, K.; Fujiwara, A.; Harada, I.; Kotani, A. X-Ray Magnetic Circular Dichroism at Rare-Earth L_{23} Absorption Edges in Various Compounds and Alloys. *Phys. Rep.* **2006**, *431*, 1−38.
(31) Kurz, P.; Bihlmayer, G.; Blügel, S. Magnetism and Electronic Structure of Hcp Gd and the Gd(0001) Surface. *J. Phys.: Condens. Matter* **2002**, *14*, 6353−6371.
(32) Gambardella, P.; Rusponi, S.; Veronese, M.; Dhesi, S. S.; Grazioli, C.; Dallmeyer, A.; Cabria, I.; Zeller, R.; Dederichs, P. H.; Kern, K.; Carbone, C.; Brune, H. Giant Magnetic Anisotropy of Single Cobalt Atoms and Nanoparticles. *Science* **2003**, *300*, 1130−1133.
(33) Shick, A. B.; Pickett, W. E.; Fadley, C. S. Electron Correlation Effects and Magnetic Ordering at the Gd(0001) Surface. *Phys. Rev. B: Condens. Matter Mater. Phys.* **2000**, *61*, R9213−R9216.
(34) Schütz, G.; Knülle, M.; Wienke, R.; Wilhelm, W.; Wagner, W.; Kienle, P.; Frahm, R. Spin-Dependent Photoabsorption at Thel-Edges of Ferromagnetic Gd and Tb Metal. *Z. Phys. B: Condens. Matter* **1988**, *73*, 67−75.
(35) Carra, P.; Harmon, B. N.; Thole, B. T.; Altarelli, M.; Sawatzky, G. A. Magnetic X-Ray Dichroism in Gadolinium Metal. *Phys. Rev. Lett.* **1991**, *66*, 2495−2498.
(36) Fischer, P.; Schütz, G.; Stähler, S.; Wiesinger, G. Investigation of the Systematics of Cmxd at the $L_{2,3}$ Edges in $(Re)_2co_{17}$. *J. Appl. Phys.* **1991**, *69*, 6144−6146.
(37) Leuenberger, F.; Parge, A.; Felsch, W.; Baudelet, F.; Giorgetti, C.; Dartyge, E.; Wilhelm, F. X-Ray Magnetic Circular Dichroism at the Gd $L_{2,3}$ Absorption Edges in Gdn Layers: The Influence of Lattice Expansion. *Phys. Rev. B: Condens. Matter Mater. Phys.* **2006**, *73*, 214430.
(38) Goedkoop, J. B.; Rogalev, A.; Rogaleva, M.; Neumann, C.; Goulon, J.; van Veenendaal, M.; Thole, B. T. Strong Final State Effects in $L_{2,3}$ Xmcd of Ionic Rare Earth Materials. *J. Phys. IV* **1997**, *7*, C2-415−C412-420.
(39) Fernandes, E.; Donati, F.; Patthey, F.; Stavrić, S.; Šljivančanin, Ž.; Brune, H. Adsorption Sites of Individual Metal Atoms on Ultrathin Mgo(100) Films. *Phys. Rev. B: Condens. Matter Mater. Phys.* **2017**, *96*, 045419.
(40) Fernandes, E. Adsorption Sites of Metal Atoms on Mgo Thin Films and Rotational Quantum State Spectroscopy of Physisorbed H_2. *Ph.D. Thesis*; EPFL: Lausanne, 2017.
(41) Pacchioni, G.; Freund, H. Electron Transfer at Oxide Surfaces. The Mgo Paradigm: From Defects to Ultrathin Films. *Chem. Rev.* **2013**, *113*, 4035−4072.
(42) Singha, A.; Baltic, R.; Donati, F.; Wäckerlin, C.; Dreiser, J.; Persichetti, L.; Stepanow, S.; Gambardella, P.; Rusponi, S.; Brune, H. ; 4f-Occupancy and Magnetism of Rare-Earth Atoms Adsorbed on Metal Substrates. *Phys. Rev. B: Condens. Matter Mater. Phys.* **2017**, *96*, 224418.
(43) Dubrovin, V.; Popov, A. A.; Avdoshenko, S. M. Valence Electrons in Lanthanide-Based Single-Atom Magnets: A Paradigm Shift in 4f-Magnetism Modeling and Design. *Inorg. Chem. Front.* **2021**, *8*, 2373−2384.
(44) Singha, A.; Willke, P.; Bilgeri, T.; Zhang, X.; Brune, H.; Donati, F.; Heinrich, A. J.; Choi, T. Engineering Atomic-Scale Magnetic Fields by Dysprosium Single Atom Magnets. *Nat. Commun.* **2021**, *12*, 4179.
(45) Paul, W.; Yang, K.; Baumann, S.; Romming, N.; Choi, T.; Lutz, C. P.; Heinrich, A. J. Control of the Millisecond Spin Lifetime of an Electrically Probed Atom. *Nat. Phys.* **2017**, *13*, 403−407.
(46) Abragam, A.; Bleaney, B. *Electron Paramagnetic Resonance of Transition Ions*; Clarendon P.: Oxford, 1970.
(47) Singha, A.; Donati, F.; Wäckerlin, C.; Baltic, R.; Dreiser, J.; Pivetta, M.; Rusponi, S.; Brune, H. Magnetic Hysteresis in Er Trimers on Cu(111). *Nano Lett.* **2016**, *16*, 3475−3481.
(48) Singha, A.; Donati, F.; Natterer, F. D.; Wäckerlin, C.; Stavric, S.; Popovic, Z. S.; Sljivancanin, Z.; Patthey, F.; Brune, H. Spin Excitations in a 4f-3d Heterodimer on Mgo. *Phys. Rev. Lett.* **2018**, *121*, 257202.
(49) Westerstrom, R.; Uldry, A. C.; Stania, R.; Dreiser, J.; Piamonteze, C.; Muntwiler, M.; Matsui, F.; Rusponi, S.; Brune, H.; Yang, S.; Popov, A.; Buchner, B.; Delley, B.; Greber, T. Surface Aligned Magnetic Moments and Hysteresis of an Endohedral Single-Molecule Magnet on a Metal. *Phys. Rev. Lett.* **2015**, *114*, 087201.
(50) Chen, C. H.; Spree, L.; Koutsouflakis, E.; Krylov, D. S.; Liu, F.; Brandenburg, A.; Velkos, G.; Schimmel, S.; Avdoshenko, S. M.; Fedorov, A.; Weschke, E.; Choueikani, F.; Ohresser, P.; Dreiser, J.; Büchner, B.; Popov, A. A. Magnetic Hysteresis at 10 K in Single Molecule Magnet Self-Assembled on Gold. *Adv. Sci.* **2021**, *8*, 2000777.
(51) Studniarek, M.; Wäckerlin, C.; Singha, A.; Baltic, R.; Diller, K.; Donati, F.; Rusponi, S.; Brune, H.; Lan, Y.; Klyatskaya, S.; Ruben, M.; Seitsonen, A. P.; Dreiser, J. Understanding the Superior Stability of Single-Molecule Magnets on an Oxide Film. *Adv. Sci.* **2019**, *6*, 1901736.
(52) Baltic, R.; Donati, F.; Singha, A.; Wäckerlin, C.; Dreiser, J.; Delley, B.; Pivetta, M.; Rusponi, S.; Brune, H. Magnetic Properties of Single Rare-Earth Atoms on Graphene/Ir(111). *Phys. Rev. B: Condens. Matter Mater. Phys.* **2018**, *98*, 024412.
(53) Pivetta, M.; Rusponi, S.; Brune, H. Direct Capture and Electrostatic Repulsion in the Self-Assembly of Rare-Earth Atom Superlattices on Graphene. *Phys. Rev. B: Condens. Matter Mater. Phys.* **2018**, *98*, 115417.
(54) Piamonteze, C.; Flechsig, U.; Rusponi, S.; Dreiser, J.; Heidler, J.; Schmidt, M.; Wetter, R.; Calvi, M.; Schmidt, T.; Pruchova, H.; Krempasky, J.; Quitmann, C.; Brune, H.; Nolting, F.; Treme Beamline at Sls, X-. X-Ray Magnetic Circular and Linear Dichroism at High Field and Low Temperature. *J. Synchrotron Radiat.* **2012**, *19*, 661−674.
(55) Giannozzi, P.; Andreussi, O.; Brumme, T.; Bunau, O.; Buongiorno Nardelli, M.; Calandra, M.; Car, R.; Cavazzoni, C.; Ceresoli, D.; Cococcioni, M.; Colonna, N.; Carnimeo, I.; Dal Corso, A.; de Gironcoli, S.; Delugas, P.; DiStasio, R. A.; Ferretti, A.; Floris, A.; Fratesi, G.; Fugallo, G.; et al. Advanced Capabilities for Materials Modelling with Quantum Espresso. *J. Phys.: Condens. Matter* **2017**, *29*, 465901.
(56) Prandini, G.; Marrazzo, A.; Castelli, I. E.; Mounet, N.; Marzari, N. Precision and Efficiency in Solid-State Pseudopotential Calculations. *Npj Comput. Mater.* **2018**, *4*, 72.
(57) Monkhorst, H. J.; Pack, J. D. Special Points for Brillouin-Zone Integrations. *Phys. Rev. B* **1976**, *13*, 5188−5192.
(58) Haverkort, M. W. Quanty for Core Level Spectroscopy - Excitons, Resonances and Band Excitations in Time and Frequency Domain. *J. Phys.: Conf. Ser.* **2016**, *712*, 012001.
(59) Cowan, R. D. *The Theory of Atomic Structure and Spectra*; University of California Press: Berkeley, 1981.
(60) Goeller-Walrand, C.; Binnemans, K., Rationalization of Crystal-Field Parametrization. In *Handbook on the Physics and Chemistry of Rare Earths*; Gschneidner, K. A. J., Eyring, L., Eds.; Elsevier: Amsterdam, 1996; Vol. 23, pp 121−283.
(61) Uldry, A.; Vernay, F.; Delley, B. Systematic Computation of Crystal-Field Multiplets for X-Ray Core Spectroscopies. *Phys. Rev. B: Condens. Matter Mater. Phys.* **2012**, *85*, 125133.

https://doi.org/10.1021/acsnano.1c05026
ACS Nano 2021, 15, 16162−16171

Supporting Information for "Mapping Orbital-Resolved Magnetism in Single Lanthanide Atoms"

Aparajita Singha[1,2,3,‡], Daria Sostina[1,2,‡], Christoph Wolf [1,2,‡], Safa L. Ahmed[1,4], Denis Krylov[1,2], Luciano Colazzo[1,2], Pierluigi Gargiani[5], Stefano Agrestini[5], Woo-Suk Noh[6], Jae-Hoon Park[7], Marina Pivetta[8], Stefano Rusponi[8], Harald Brune[8], Andreas J. Heinrich[1,4], Alessandro Barla[9], and Fabio Donati[1,4,]*

[1]Center for Quantum Nanoscience, Institute for Basic Science (IBS), Seoul 03760, Republic of Korea

[2]Ewha Womans University, Seoul 03760, Republic of Korea

[3]Max Planck Institute for Solid State Research, Stuttgart 70569, Germany

[4]Department of Physics, Ewha Womans University, Seoul 03760, Republic of Korea

[5]ALBA Synchrotron Light Source, Cerdanyola del Vallès, 08290, Catalonia, Spain

[6]MPPC-CPM, Max Planck POSTECH/Korea Research Initiative, Pohang 37673, Korea

[7]Department of Physics, Pohang University of Science and Technology (POSTECH), Pohang 37673, Korea

[8]Institute of Physics, École Polytechnique Fédérale de Lausanne, Station 3, CH-1015 Lausanne, Switzerland

[9]Istituto di Struttura della Materia (ISM), Consiglio Nazionale delle Ricerche (CNR), I-34149

Trieste, Italy

Content of the Supporting Information

Background subtraction in X-ray absorption spectra

In order to compare the shape of the X-ray absorption (XAS) and magnetic circular dichroism (XMCD) spectra measured on different samples, we performed the following analysis. First, all spectra were subtracted from a respective background profile, which was acquired prior to the deposition of the rare earth atoms on the MgO substrate, without changing any other experimental parameters. The background subtracted absorption signals are shown in **Figure S1**a and **S1**c for M_3 and M_2 absorption edges respectively, from 0.14 ML Gd on MgO/Ag(100). Note that the XAS of background and atoms were normalized such that they match at the two ends of the spectral range for the corresponding X-ray polarization. Second, the baseline of thus obtained absorption spectra exhibited a step-like feature as evident in **Figure S1**b and **S1**d. Very similar behavior has been previously observed for $L_{2,3}$ edges of Gd.[1] This step originates from non-resonant excitations, namely when the core electrons are excited with sufficient energies allowing access to the continuum of unoccupied states. Note that this effect is less evident for the $M_{4,5}$ edges as the signal from the corresponding resonant absorption edge dominates the overall spectral shape.

For all edges, we subtracted this step profile by fitting the total absorption, defined by the sum of the signals from two circular polarizations, with the following function:

$$f(x) = a + b * x + c * x^2 + d * \left[1 - \frac{1}{1+\exp\left(\frac{x-e}{w}\right)}\right] \quad \text{(S1)}$$

Here *a*, *b*, *c*, *d* and *e* are fitting parameters, while *w* is the step-width, which was chosen to be 7 eV for both Gd and Ho for $M_{1,2,3}$ absorption edges. This allowed us to obtain an almost featureless background for all energies except for the position of the respective absorption peak. The remaining post-edge oscillatory absorption profile comes from extended X-ray absorption fine structure. An example of subtracting such a step profile is shown in **Figure S1**b and **S1**d for M_3 and M_2 edges data acquired from 0.14 ML Gd on MgO/Ag(100). Finally, to compare the spectral shape of XMCD from different atom and cluster samples we normalized all spectra to the integrated XAS at the $M_{4,5}$ edge measured on the same sample.

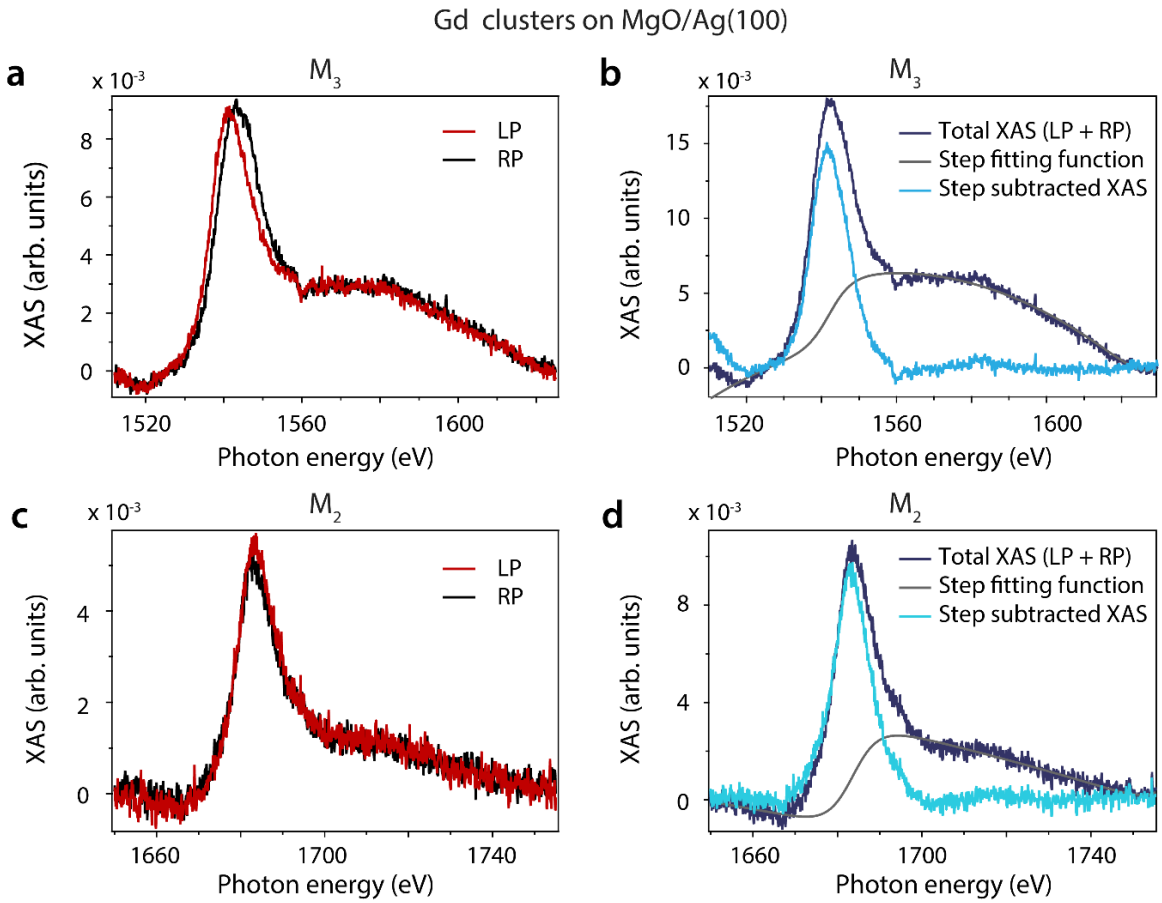

Figure S1. Background subtraction at the $M_{2,3}$ edges**.** (a) Left (LP) and right polarization (RP) XAS signal of the M_3 edge of Gd clusters on MgO/Ag(100) after subtraction of the bare MgO/Ag(100) background signal. (b) The total XAS signal obtained by summing LP and RP from (a) is shown together, with a step fitting function. The resulting step subtracted XAS is also shown. (c-d) Same procedure of (a) and (b) is reported for the M_2 edge. All measurements are performed in grazing incidence (Gd coverage Θ_{Gd} = 0.14 ML, B = 5 T, T = 6.5 K).

Angle-dependent measurements of Gd on MgO/Ag(100)

We performed further characterization of the magnetism of Gd atoms and clusters on MgO/Ag(100) by angle-dependent XAS and XMCD measurements. As shown in **Figure S2**a and **S2**b, the Gd spectra at the $M_{4,5}$ edges at the maximum available field are essentially identical along the two indicated directions, namely normal incidence (photon beam and magnetic field normal to the sample surface) and grazing incidence (both photon beam and field at 60 degrees from surface normal). Magnetization loops along the two directions show slight differences, with a weak out-of-plane easy axis, see **Figure S2**c. The weak anisotropy is a general property of half-filled 4f shell, with the total charge close to spherical symmetry.[2] The anisotropy stems from the strong crystal field that induces mixing with higher multiplets, resulting in a non-vanishing value of the 4f orbital angular momentum of $\langle L_z \rangle = 0.14 \pm 0.05\ \mu_B$ parallel to the spin moment, as obtained from sum rules. The sign and magnitude of the orbital moment is correctly captured by our multiplet calculations $\langle L_z \rangle_{multiplet} = 0.04\ \mu_B$.

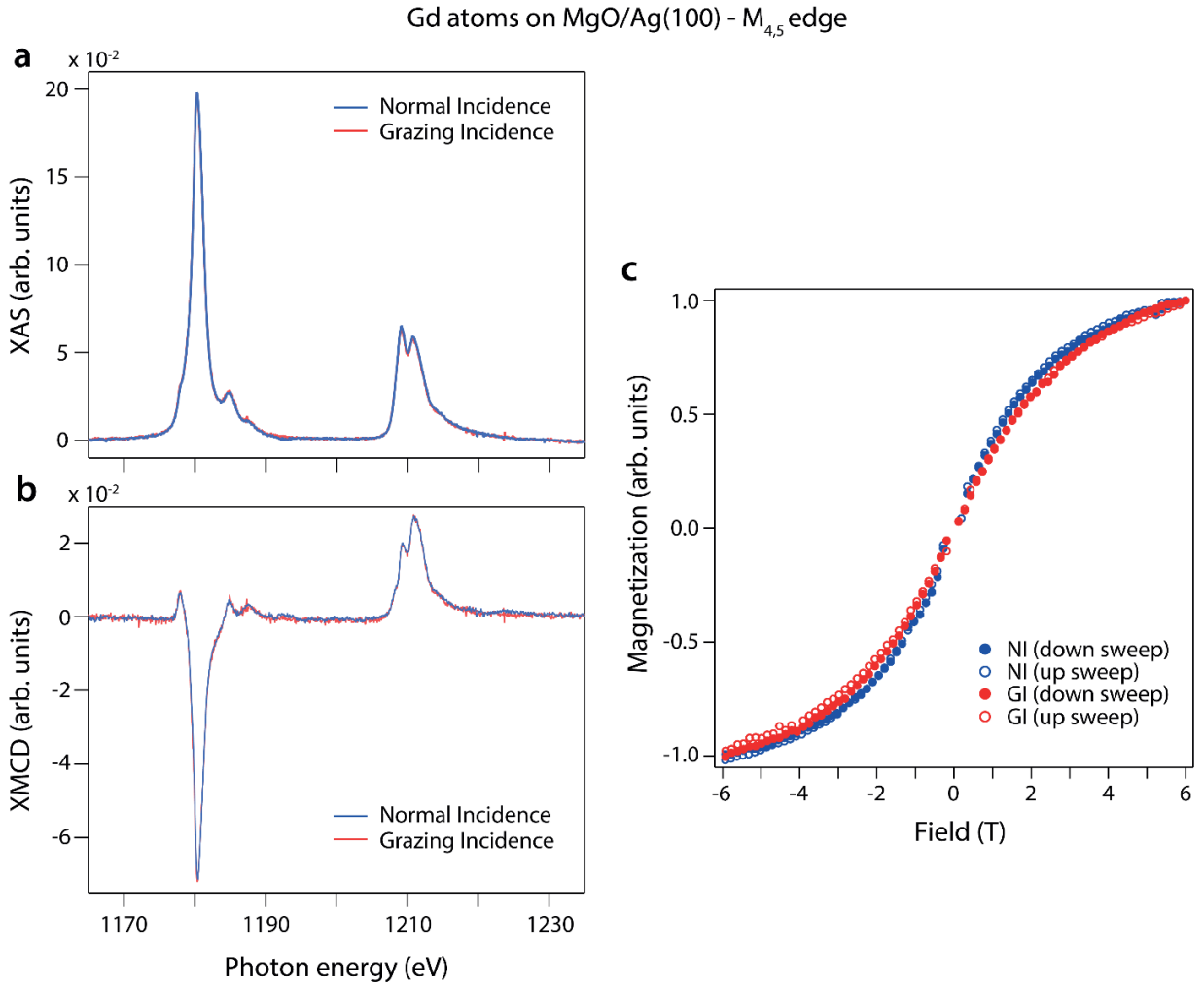

Figure S2. Anisotropy of Gd atoms on MgO/Ag(100). (a) XAS and (b) XMCD measurements at the $M_{4,5}$ edge of Gd for two incident angles, normal incidence (NI) and grazing incidence (GI) at B = 6 T. (c) Magnetization loops of the Gd atoms measured at the M_5 edge (Θ_{Gd} = 0.03 ML, field sweep speed dB/dt = 33 mT/s, T = 6.5 K).

Gadolinium clusters also show negligible angular anisotropy in the XAS and XMCD spectra at B = 5 T, see **Figure S3**a and **S3**b. Due to the larger absorption signal available for this sample with larger Gd coverage, we compared the amplitude of the field dependent XMCD signal obtained at the M_5 and M_3 edges (**Figure S3**c). The two signals show the same field dependence, indicating strong magnetic coupling between the 4f and 5d states. We note that even in the absence of 5d electrons in the ground state, the XMCD signal is sensitive to the magnetic coupling at the excited state,[3] which in our case is represented by an additional photoelectron promoted from the 3p to the 5d orbitals.

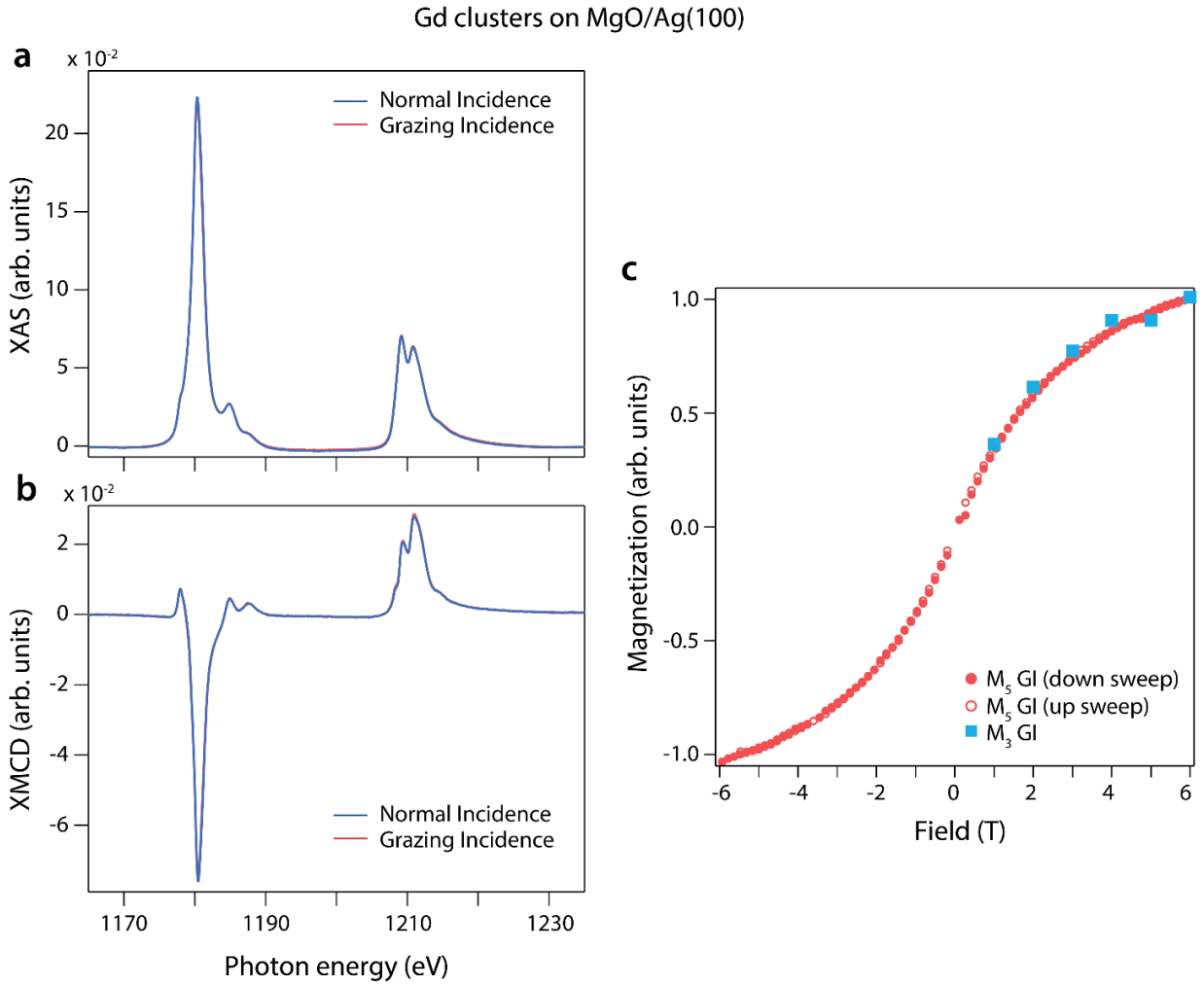

Figure S3. Anisotropy of Gd clusters on MgO/Ag(100). (a) XAS and (b) XMCD measurements at the $M_{4,5}$ edge of Gd for two incident angles, normal incidence (NI) and grazing incidence (GI) at B = 5 T. (c) Magnetization loops of the Gd clusters measured at the M_5 and M_3 edges in GI (Θ_{Gd} = 0.14 ML, dB/dt = 33 mT/s, T = 6.5 K).

Additional details on M_1 edge of Gd clusters on MgO/Ag(100)

Due to the absence of spin-orbit coupling at the 3s core level, measurements at the M_1 edge of lanthanides cannot directly probe the spin moment, hence only orbital moment contributes to the XMCD at this edge. Our calculations show that a $6p^1$ configuration should result in a rather large angular momentum of $\langle L_z \rangle_{6p^1} = 0.7\ \mu_B$ for the atoms and gives a characteristic XMCD signal at the M_1 edge, as shown in **Figure S4**. Even if the multiplet spectra of atoms and experiment of Gd clusters are not directly comparable, our data do not show any relevant feature beyond the noise level suggesting a vanishing orbital moment on the Gd clusters at the 6p orbital. Since atoms showing large values of orbital moment are normally likely to have finite orbital moment even in atomic-scale clusters,[4] a spin polarization at the 6p states should result in a non-vanishing orbital moment and a finite XMCD area at the M_1 edge. Therefore, even if the M_1 edge is not directly probing the spin magnetic moment, the absence of visible line shapes suggests a vanishing orbital moment, which according to our model indirectly implies the absence of unpaired electrons.

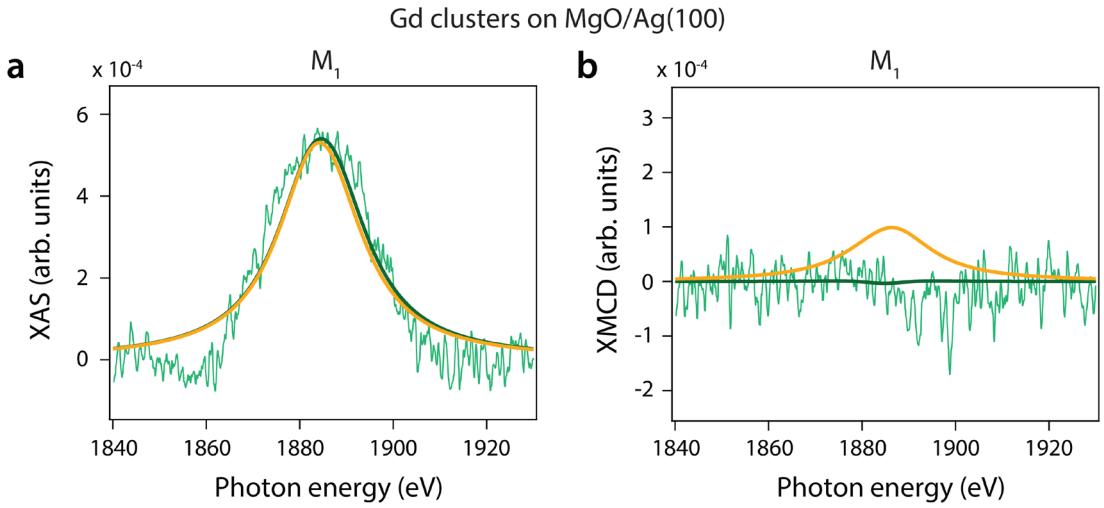

Figure S4. M_1 edge of Gd clusters on MgO/Ag(100). (a) XAS and (b) XMCD measurements at the M_1 edge of Gd clusters at B = 5 T. (Θ_{Gd} = 0.14 ML, T = 6.5 K). Corresponding XAS XMCD signals are compared to simulations for both $6p^0$ (dark green solid line) and $6p^1$ (orange solid line) configurations.

XAS and XMCD of Gd film on MgO/Ag(100)

A gadolinium film of 1.2 ML has been prepared by depositing on a sample with a MgO film grown on Ag(100). The Gd deposition has been performed by keeping the sample at RT in a base pressure of $1x10^{-9}$ mbar. The corresponding XAS and XMCD spectra at the $M_{2,3}$ edges are shown in **Figure S5**. To compare the XMCD of the Gd film with that of the atoms and clusters, we show the related XMCD spectra and integrated XMCD signal normalized by the corresponding total XAS in Fig. **S6**. Although minor differences are visible on the spectra, we observe clear trends in the integrated signals, which are more sensitive to minute deviation of the spectral shapes and weights.[4] At the M_3 edge, the integrated XMCD goes from positive to negative going from atoms, to clusters and to the film. The trend is less neat at the M_2 edge, for which the integrated value of atoms and clusters are very similar. Nevertheless, the film shows a rather different value of the integrated

signal beyond our noise level. The value of the integrated XMCD is reported in **Figure 3**f and **3**g of the main text.

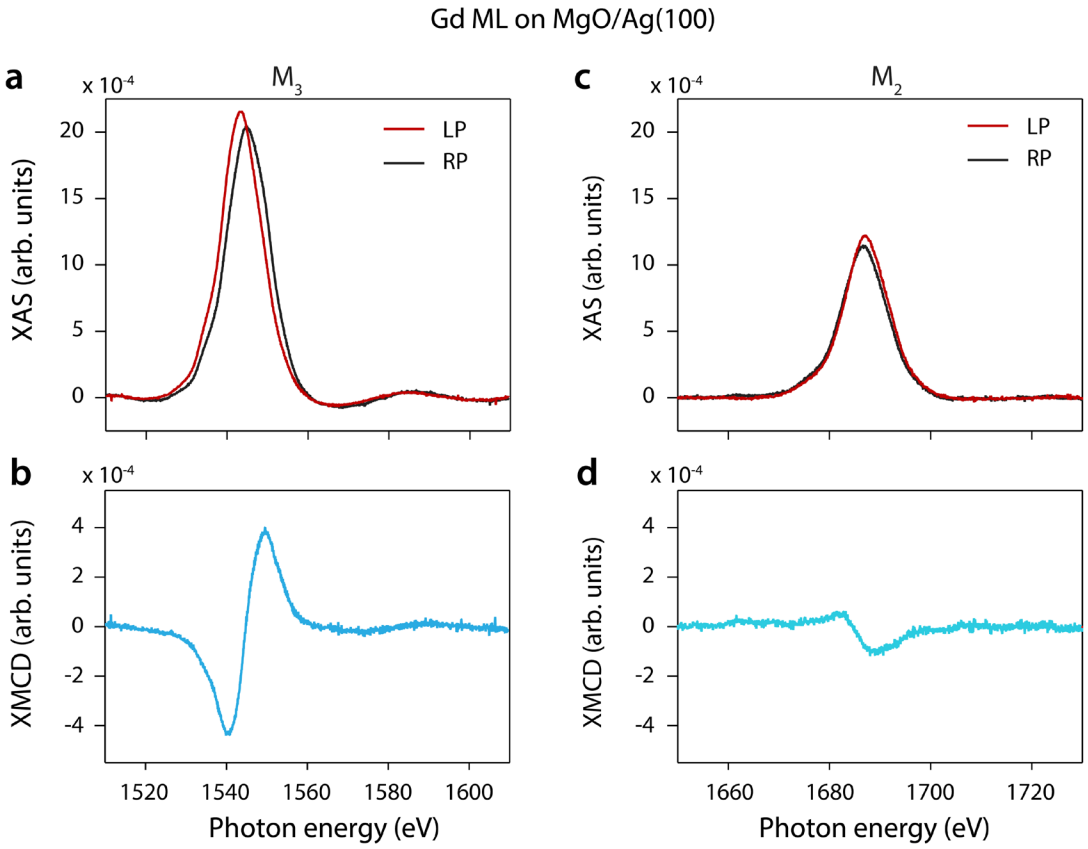

Figure S5. Spectra at the $M_{2,3}$ edges of Gd film on MgO/Ag(100). (a) XAS and (b) XMCD measurements at the M_3 edge of Gd. **c-d** Same for the M_2 edge. (Θ_{Gd} = 1.2 ML, T = 2.5 K, B = 6.8 T).

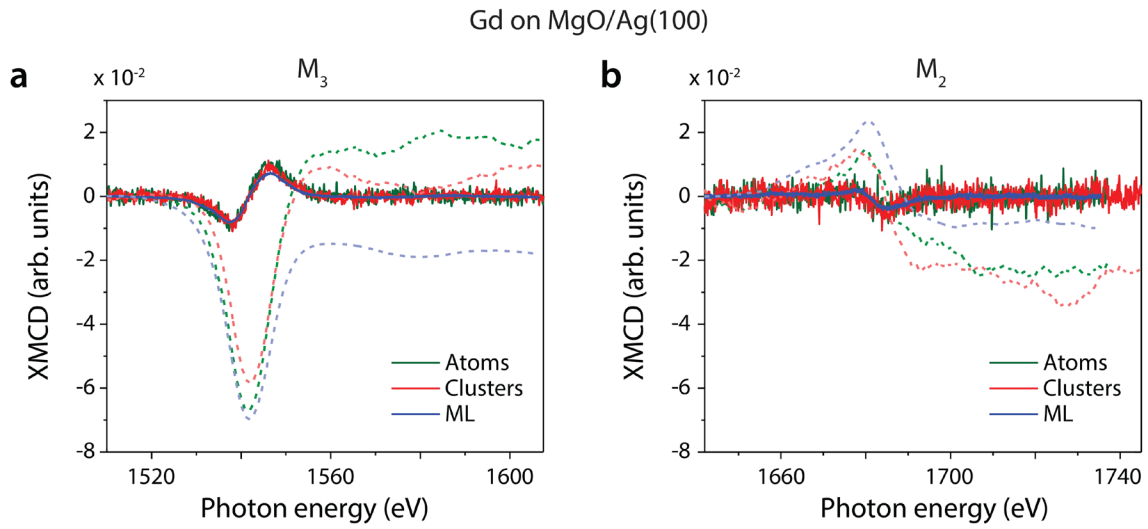

Figure S6. XMCD at the $M_{2,3}$ edges of Gd atoms, clusters, and film on MgO/Ag(100). (a) XMCD spectra at the M_3 edge normalized to the total XAS for Gd atoms, clusters and film on MgO/Ag(100). (b) XMCD spectra at the M_2 edge of Gd. The evolution of the integrated XMCD with the photon energy is shown with dashed lines of the corresponding color.

Reference measurements on Gd(III) sulfate octahydrate

Due to its well-known chemical valence and paramagnetic behavior down to low temperatures, Gd(III) sulfate octahydrate is a suitable reference sample to test $M_{2,3}$ transitions in a system with depleted valence 5d, 6s and 6p orbitals.[5] Previous electron spin resonance measurements of Gd(III) sulfate octahydrate found no indications of unpaired spins in the outer shells of Gd.[6] In this material, the strong chemical ligand leaves the Gd in a chemical trivalent state, with the total contribution to the magnetic moment coming only from the half-filled 4f electrons. For this system, a clear signal from a $5d^0$ configuration is expected at the $M_{2,3}$ edges.

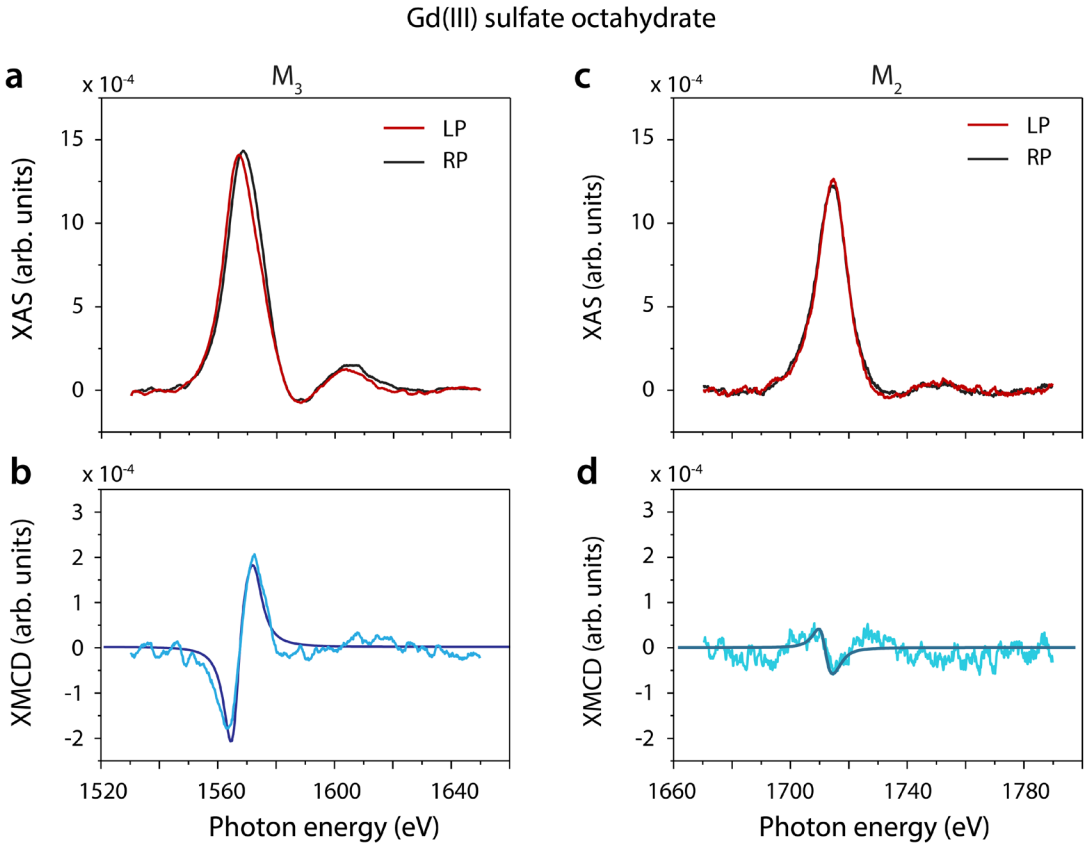

Figure S7. Reference XAS and XMCD spectra of Gd(III) sulfate octahydrate. (a) XAS and (b) XMCD measurements at the M_3 edge of Gd. (c-d) Same for the M_2 edge (T = 15 K, B = 6.0 T). In panels (b) and (d), the simulated XMCD signal from multiplet calculations is shown with darker lines.

The XAS and XMCD spectra of this material were acquired at the 6A MeXiM beamline at Pohang Light Source-II. The sample was prepared by dissolving the Gd salts in pure water, drop casting the solution on the bare copper sample plate, and inserted in the measurement chamber. For that experimental setup, comparative measurements on $DySc_2N@C_{82}$ fullerenes powder[7] indicate a base temperature of 15 K at the sample plate. Spectra at the $M_{2,3}$ edges acquired at 6.0 T (**Figure S7**) show line shape features that are very similar to those of Gd atoms and clusters on MgO/Ag(100), see **Figure 2** and **3** of the main text. The M_3 edge shows a pronounced peak derivative shape, while a shallow dip is observed at the M_2. In order to simulate the spectra with multiplet calculations, we performed DFT calculations of the system to obtain the CF splitting of the 5d orbitals of the Gd atoms, see **Table S1**. We then simulate the expected powder spectrum by summing over 6 discrete possible orientations of the Gd principal axis. As also done in Fig. 3 of the main text, the sum of the two polarizations is matched to the total experimental XAS. The comparison between experiment and simulated XMCD is shown in Fig. S7. The electrically and thermally insulating character of the sample is responsible for the larger noise and background fluctuations on that sample, however, the agreement with the calculations is convincingly supporting the reliability of the multiplet calculations in this analysis XMCD spectra at the $M_{2,3}$ edges.

Multiplet calculations of the $L_{2,3}$ edges

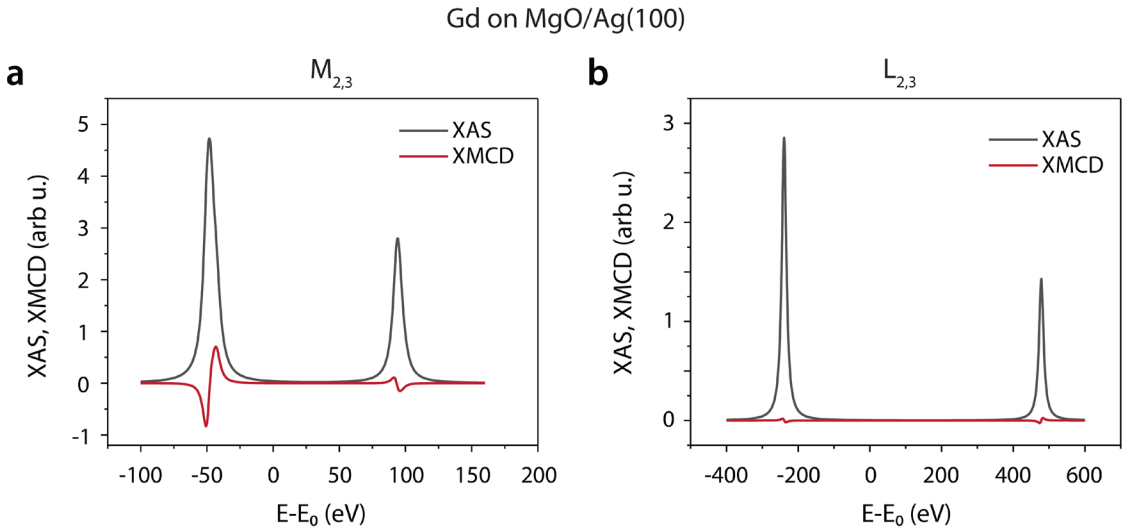

Figure S8. Calculated $M_{2,3}$ and $L_{2,3}$ spectra of Gd atoms on MgO/Ag(100). (a) Calculated XAS and XMCD measurements at the $M_{2,3}$ edge of Gd and (b) at the $L_{2,3}$ edges. The energy scale is reported as difference with respect to the center of mass of the spectral weight (E_0).

Spectra at the $L_{2,3}$ edges of Gd atoms on MgO have been simulated using multiplet calculations. We assumed identical crystal field and rescaling factors of the slater integrals as found for the $M_{2,3}$ edges. To include the shorter lifetime of the excited states, the line broadening at the $L_{2,3}$ (20 eV) is taken to be double than that of the $M_{2,3}$ (10 eV). The comparison between these edges is shown in **Figure S8**. Despite the identical $5d^0$ electronic configuration, the calculated XMCD signal at the $L_{2,3}$ is about 30 times smaller than at the $M_{2,3}$. As mentioned in the main text, this stems from the 2p-4f coupling that is about 6 times weaker than for the 3p-4f. This reduced interaction affects the intensity of the $L_{2,3}$ XMCD *via* the indirect 4f-2p-5d coupling. In this situation, the weak derivative signal from atomic-like dipolar transitions is possibly overwhelmed by the asymmetric signal of the breathing effect, not considered in our calculations, which determines the shape and intensity of the XMCD at the $L_{2,3}$ edges.

Details of DFT calculations

- Orbital-resolved charge analysis of the Gd atoms

Additional insight into the orbital hybridization can be obtained by analyzing the projected density of states (PDOS) for the Gd, O and Mg orbitals shown in **Figure S9**. Due to the very weak hybridization occurring on the 4f electrons, these states are not presented in those plots. For both Gd/MgO and Gd/MgO/Ag(100) we observe a set of well separated states in the region around the Fermi level. We observe a spin split pair of states indicated with a violet dashed box in **Figure S9**b and **S9**d to have dominant 6s character. Due to the large radial function of the 6s orbitals, this state is strongly hybridized with p states of the neighboring Mg atoms, see **Figure S9**a and **S9**c. Additional on-site hybridization provides a slight d_{z^2} and p_z character to the states, with a related occupation of about 0.21 and 0.09 electrons, respectively, both with very small net spin polarization. Hence, we expect these states to give negligible contribution to the $M_{1,2,3}$ XMCD edges. The multi-orbital character of this state deforms the original 6s spherical symmetry, as shown in the charge density plot of **Figure S10**a and **S10**c.

The state indicated with a black dashed box is also particularly relevant, as its occupation strongly depends on the presence/absence of the underneath Ag substrate. In both systems, this state has a strong atomic-like $5d_{x^2-y^2}$ character. We find only little hybridization with the Mg p orbitals of the neighboring atoms towards which the 5d orbital lobes are oriented, see also **Figure S10**b and **S10**d. Due to its almost full spin polarization, this state is expected to give a large contribution to the XMCD signal of the $M_{2,3}$ edges. In addition, the localized nature of this state supports the use of multiplet analysis to interpret the XAS and XMCD spectra and infer the depletion.

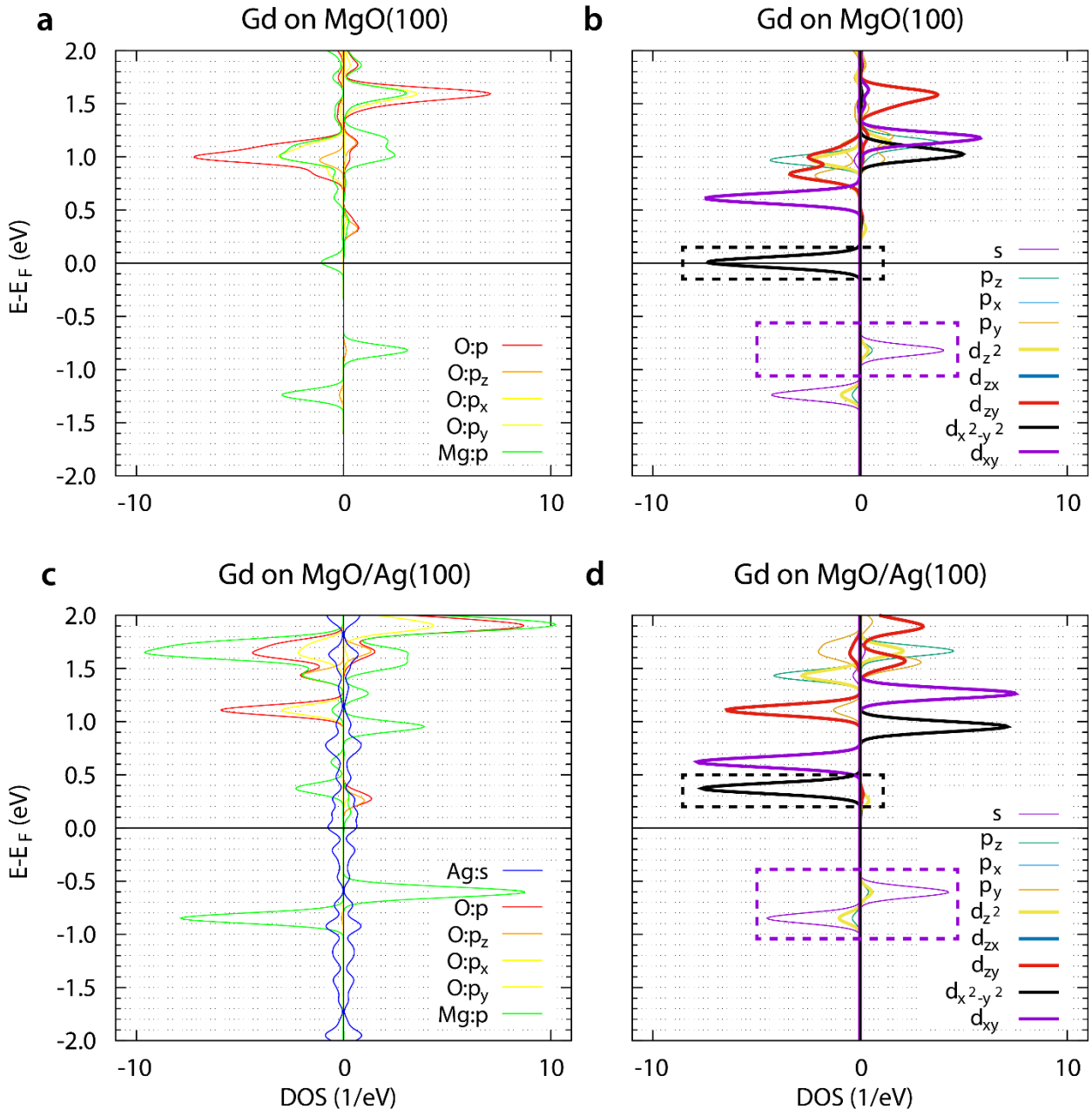

Figure S9. Orbital analysis of the Gd adatoms. (a) PDOS of O and Mg orbitals for Gd on MgO(100). (b) PDOS of 6s, 6p, and 5d orbitals of Gd on MgO(100). (c-d) PDOS for the Gd on MgO/Ag(100) system. All plots are broadened for visual purposes with a Gaussian of approximately 0.1 eV.

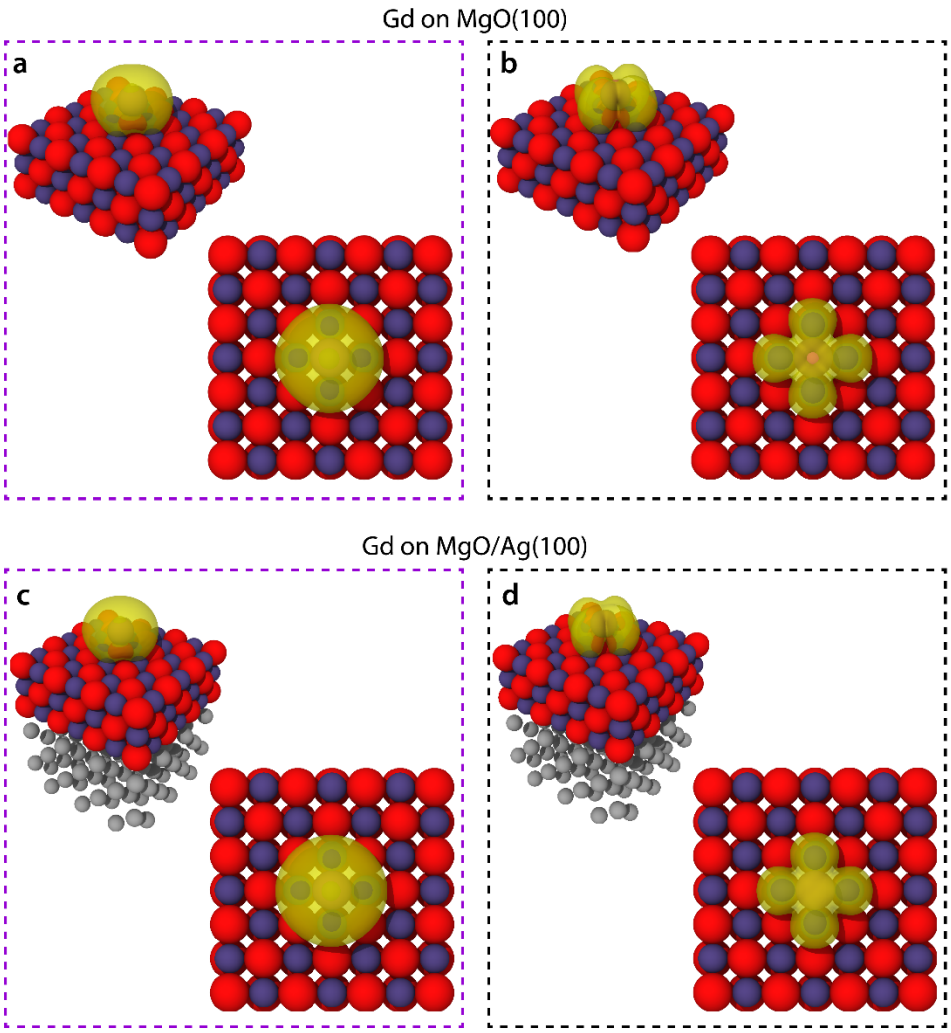

Figure S10. Integrated densities of Gd states close to Fermi energy. (a) Side and top view of states with 6s – like character for the Gd on MgO(100) (purple dashed box of **Figure S9**b). (b) Side and top view of states with $5\mathbf{d}_{\mathbf{x^2-y^2}}$ character for the Gd on MgO(100) (black dashed box of **Figure S9**b). (c) and (d) 6s-like and $5\mathbf{d}_{\mathbf{x^2-y^2}}$-like states for the Gd on MgO/Ag(100) system obtaind by plotting the states in purple and black dashed boxes, respectively, indicated in **Figure S9**d. In the plots, red, violet and grey spheres represent O, Mg, and Ag atoms, respectively, whereas the yellow contours are electron states isosurfaces of the indicated PDOS with a value of 0.001.

- Evaluation of crystal field parameters from DFT calculations

We tested two complementary approaches to extract the crystal field (CF) splitting: (i) by diagonalization of the full DFT Hamiltonian and (ii) by construction of maximally localized Wannier functions (MLWFs) of a non-spin-polarized DFT calculation.[8] It has been observed that the former will yield a larger CF splitting due to covalent contribution to the total energy, whereas the latter is reduced by about 70%.[9, 10] For the Wannierization procedure we included projections

for Gd:p and d and O:p orbitals. Disentanglement was used to extract isolated bands within a window of 3 eV of the Gd:5d bands. All calculations were performed with the Wannier90 code.[11] We found that both approaches yield CFs that result in comparable simulated spectra as the results of the multiplet calculations are not very sensitive to the CF splitting of the empty $5d^0$ orbitals. This, conversely, also means that systematic underestimation of CF splitting for empty states as can be expected from approximate DFT due to the self-interaction error are not expected to play a role here. The crystal field parameters are given in **Table S1**. Additional calculations of Mg-substitutional Gd in bulk MgO indicate that the e_g-t_{2g} splitting amounts to 6.4 (4.5) eV for DFT (MLWFs). Hence, the CF splitting for the adatom is drastically reduced compared to bulk case.

Table S1. CF splitting parameters for the 5d orbitals of Gd on MgO/Ag(100). Given are the dominant orbital character and the energy obtained directly from DFT or by MLWFs. For the former, the energies are obtained from the peaks of the non spin-polarized PDOS.

Orbital	Energy (eV) (DFT)	Energy (eV) (MLWFs)
d_{z^2}	0.268	0.182
d_{zx}	0.318	0.220
d_{zy}	0.318	0.220
$d_{x^2-y^2}$	-0.602	-0.418
d_{xy}	-0.282	-0.197
Total split:	**0.92**	**0.64**

Additional data for Ho atoms on MgO/Ag(100)

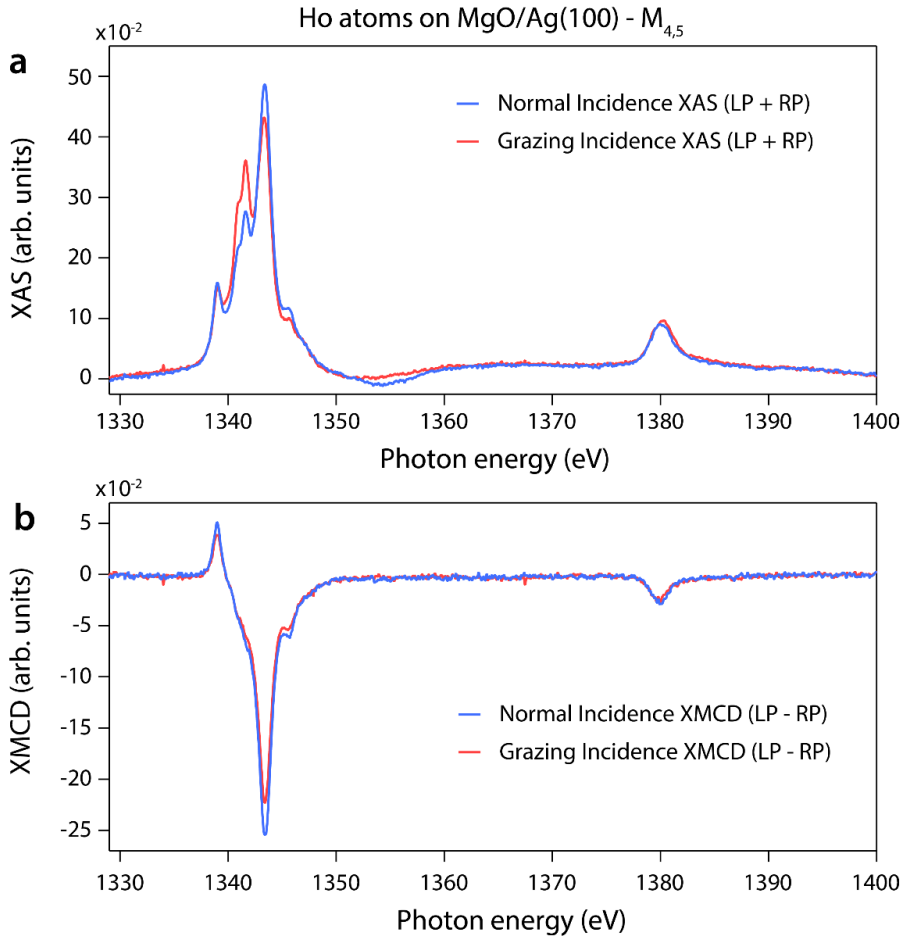

Figure S11. X-ray spectra at the $M_{4,5}$ edges of Ho atoms on MgO/Ag(100). (a) XAS and (b) XMCD signals of Ho atoms at the two indicated incidence geometries (Θ_{Ho} = 0.03 ML B= 6 T, T = 6.5 K).

Measurements of the $M_{4,5}$ edges of 0.03 ML of Ho deposited on MgO/Ag(100) are shown in **Figure S11**. The characteristic shape of the spectrum is rather different than that of Ho on bare Ag(100)[12] and allows us to identify its $4f^{10}$ occupation.[12-14] Differently from Gd, Ho shows a pronounced anisotropy in both XAS and XMCD which is characteristic of the interaction with the strong ligand field provided by the MgO surface, in particular at the oxygen-top binding site.[14] The line shape and anisotropy at these edges compares very well with previous data.[14, 15] Minor discrepancies can be attributed to the slightly larger Ho coverage used in this experiment, which may have triggered some amount of cluster nucleation on the surface.

Parameters for multiplet calculations

As discussed in the Method section of the main text, the Slater integrals to model the electron-electron interaction have been computed with the Cowan's atomic structure code[16] and rescaled to fit the experimental spectra. For Gd, all parameters have been rescaled to 0.7 to fit the $M_{4,5}$ spectrum, while an unscaled value of the 3p-4f integral is required to match the amplitude of the XMCD signal at the M_3 edge. As discussed in the text, this parameter indirectly couples the 4f to the 5d through a 4f-3p-5d exchange. Due to this coupling, a finite positive value of the XMCD integral at the M_3 edge is predicted even in absence of 5d electrons. For Ho, all parameters have been rescaled according to previous values.[12] **Table S2** summarizes the values used for Gd and Ho. These values are in line with previous results obtained for lanthanide atoms on surfaces.[12-14, 17]

Table S2. Rescaling parameters for the Slater integrals for multiplet calculations. The coefficients rescale the computed values from the Cowan's atomic structure code.[16]

Element	**4f-4f**	**5d-5d**	**6p-6p**	**4f-5d**	**4f-6p**	**3d-4f**	**3p-4f**	**3p-5d**	**3s-4f**	**3s-6p**
Gd	0.70	0.70	0.70	0.70	0.70	0.70	1.00	0.70	0.70	0.70
Ho	0.85	0.85	0.85	0.85	0.85	0.85	0.85	0.85	0.85	0.85

The crystal field parameters for the 4f electrons have been computed from a point charge electrostatic model[18] using the position and values of the neighboring atoms obtained from DFT (see **Table S3**). The crystal field parameters in the Wybourne notation $\tilde{A}_m^n$ are shown in **Table S4** and **Table S5** for Gd and Ho, respectively. However, the expectation values $\langle r^n \rangle$ of the radial functions from the Cowan's code used to compute those values are known to underestimate the actual splitting observed in experiments.[19] Therefore, the crystal field parameters value has been rescaled to match the level splitting computed from a benchmark multiplet code (multiX).[19] The rescaling values κ_m^n as well as the final values used in the calculations $A_m^n = \kappa_m^n \tilde{A}_m^n$ are summarized in Table S4 and S5.

The crystal field parameters for the Gd 5d and 6p electrons have been computed from the energy of the 5d and 6p orbitals, respectively, calculated with DFT. The related values are summarized in **Table S6**. Identical values have been used to simulate the $M_{2,3}$ edges of Ho.

For the Gd(III) sulfate octahydrate, we simulate the crystal field acting on the 4f states using point charge model. Charges positions have been inferred from a previous crystallographic work.[20] We here adopt a symmetrized charge configuration, with the 8 coordinated oxygen to form a undistorted square antiprism. The charge positions are shown **Table S7**. The splitting of the 5d states is obtained from DFT, see **Table S1**. To match the symmetry of the point charge configuration, we symmetrize the energy position of the 5d orbitals accordingly. The related CF parameters are shown in **Table S8** and **Table S9**. The random orientation of the Gd axis in the polycrystalline sample is considered using powder spectrum averaging. Spectra at 6 azimuth angles from 15 to 90 degrees have been summed with proper angular weight. We found best agreement between experiment and simulated XMCD amplitudes assuming a sample temperature of 25 K. This temperature is higher than the expected base temperature of the sample stage of the

6A MeXiM beamline at Pohang Light Source-II, possibly due to the strong thermal insulating character of the sample that may heat up under the X-ray beam.
In this work, we neglect the effects of covalency due to the ligand field of Mg and O states, which is justified in view of the weak hybridization with the surface and the strong atomic character of the relevant 5d orbital contributing to the magnetism, both for Gd (**Figure S10**) and for Ho.[21] Adding ligand field terms to our model could possibly improve the accuracy of our results. However, for the investigated cases, the distinct shape of the lanthanide atoms' XMCD indicates a spin polarization that is much closer to that of the $5d^0$ than to the $5d^1$ scenario, suggesting a minor role of the covalency in determining the relevant magnetic properties of the system.

Table S3. Charges and positions of the neighboring ions included in the multiplet calculations. The values have been computed from DFT for Gd atom on MgO.

Ion	**Charge**	$\boldsymbol{d}_{\perp}$	$\boldsymbol{d}_{\parallel}$
O (underneath)	-2e	-215 pm	0 pm
Mg (2nd nearest neighbours)	+2e	-270 pm	208 pm
O (3rd nearest neighbours)	-2e	-270 pm	294 pm

Table S4. Crystal field parameters for the 4f electrons of Gd atoms on MgO/Ag(100). Values from the point charge model $\tilde{A}_m^n$, rescaling coefficients κ_m^n, and final parameters A_m^n are reported.

	$\tilde{A}_0^2$	$\tilde{A}_0^4$	$\tilde{A}_4^4$	$\tilde{A}_0^6$	$\tilde{A}_4^6$
	486.3 meV	102.4 meV	5.7 meV	32.7 meV	2.1 meV
	κ_0^2	κ_0^4	κ_4^4	κ_0^6	κ_4^6
Gd *4f*	$\sqrt{2}$	$2\sqrt{2}$	$2\sqrt{2}$	4	4
	A_0^2	A_0^4	A_4^4	A_0^6	A_4^6
	687.8 meV	289.7 meV	16.1 meV	130.7 meV	8.3 meV

Table S5. Crystal field parameters for the 4f electrons of Ho atoms on MgO/Ag(100). Values from the point charge model $\tilde{A}_m^n$, rescaling coefficients κ_m^n, and final parameters A_m^n are reported.

Ho 4f	$\tilde{A}_0^2$	$\tilde{A}_0^4$	$\tilde{A}_4^4$	$\tilde{A}_0^6$	$\tilde{A}_4^6$
	410.0 meV	72.2 meV	4.0 meV	18.8 meV	1.2 meV
	κ_0^2	κ_0^4	κ_4^4	κ_0^6	κ_4^6
	$\sqrt{2}$	$2\sqrt{2}$	$2\sqrt{2}$	4	4
	A_0^2	A_0^4	A_4^4	A_0^6	A_4^6
	579.8 meV	204.3 meV	11.3 meV	75.2 meV	4.8 meV

Table S6. Crystal field parameters for the 5d and 6p electrons of Gd atoms on MgO/Ag(100). Values have been computed from the Wannierization procedure. Identical values have been used for Ho.

Gd *5d*	A_0^2	A_0^4	A_4^4	Gd *6p*	A_0^2
	1470 meV	-546 meV	-401 meV		283 meV

Table S7. Charges and positions of the neighboring ions included in the multiplet calculations for Gd(III) sulfate octahydrate. The values have been extracted from previous crystallographic data[20] and symmetrized to a square antiprismatic configuration.

Ion	**Charge**	$\boldsymbol{d}_\perp$	$\boldsymbol{d}_\parallel$
O (underneath)	-2e	-197 pm	140 pm
O (above)	-2e	197 pm	140 pm

Table S8. Crystal field parameters for the 4f electrons of Gd(III) sulfate octahydrate. Values from the point charge model $\tilde{A}_m^n$, rescaling coefficients κ_m^n, and final parameters A_m^n are reported.

Gd *4f*	$\tilde{A}_0^2$	$\tilde{A}_0^4$	$\tilde{A}_0^6$
	2042 meV	322.2 meV	84.9 meV
	κ_0^2	κ_0^4	κ_0^6
	$\sqrt{2}$	$2\sqrt{2}$	4
	A_0^2	A_0^4	A_0^6
	-2888 meV	455.7 meV	120.0 meV

Table S9. Crystal field parameters for the 5d electrons of Gd(III) sulfate octahydrate. Values have been computed from the Wannierization of procedure.

Gd *5d*	A_0^2	A_0^4
	-865 meV	2005 meV

SUPPLEMENTARY REFERENCES

1. Leuenberger, F.; Parge, A.; Felsch, W.; Baudelet, F.; Giorgetti, C.; Dartyge, E.; Wilhelm, F.; X-Ray Magnetic Circular Dichroism at the Gd $L_{2,3}$ Absorption Edges in Gdn Layers: The Influence of Lattice Expansion. *Phys. Rev. B* **2006,** *73*, 214430.
2. Rinehart, J. D.; Long, J. R.; Exploiting Single-Ion Anisotropy in the Design of F-Element Single-Molecule Magnets. *Chem. Sci.* **2011,** *2*, 2078.
3. Stöhr, J.; Siegmann, H. C.; Magnetism : From Fundamentals to Nanoscale Dynamics. **2006**.
4. Gambardella, P.; Rusponi, S.; Veronese, M.; Dhesi, S. S.; Grazioli, C.; Dallmeyer, A.; Cabria, I.; Zeller, R.; Dederichs, P. H.; Kern, K.; Carbone, C.; Brune, H.; Giant Magnetic Anisotropy of Single Cobalt Atoms and Nanoparticles. *Science* **2003,** *300*, 1130-1133.
5. Levy, P. M.; Magnetic Behavior of Gadolinium Sulfate Octahydrate at Low Temperatures. *J. Chem. Phys.* **1965,** *43*, 4422-4424.
6. Tomaszewicz, E.; Leniec, G.; Kaczmarek, S. M.; Re-Investigations of Thermal Decomposition of Gadolinium Sulfate Octahydrate. *J. Therm. Anal. Calorim.* **2010,** *102*, 875-881.

7. Westerstrom, R.; Dreiser, J.; Piamonteze, C.; Muntwiler, M.; Weyeneth, S.; Brune, H.; Rusponi, S.; Nolting, F.; Popov, A.; Yang, S.; Dunsch, L.; Greber, T.; An Endohedral Single-Molecule Magnet with Long Relaxation Times: Dysc2n@C80. *J. Am. Chem. Soc.* **2012,** *134*, 9840-9843.
8. Haverkort, M. W.; Zwierzycki, M.; Andersen, O. K.; Multiplet Ligand-Field Theory Using Wannier Orbitals. *Phys. Rev. B* **2012,** *85*, 165113.
9. Ferrón, A.; Delgado, F.; Fernández-Rossier, J.; Derivation of the Spin Hamiltonians for Fe in Mgo. *New J. Phys.* **2015,** *17*, 033020.
10. Wolf, C.; Delgado, F.; Reina, J.; Lorente, N.; Efficient *ab Initio* Multiplet Calculations for Magnetic Adatoms on Mgo. *J. Phys. Chem. A* **2020,** *124*, 2318-2327.
11. Pizzi, G.; Vitale, V.; Arita, R.; Blügel, S.; Freimuth, F.; Géranton, G.; Gibertini, M.; Gresch, D.; Johnson, C.; Koretsune, T.; Ibañez-Azpiroz, J.; Lee, H.; Lihm, J.-M.; Marchand, D.; Marrazzo, A.; Mokrousov, Y.; Mustafa, J. I.; Nohara, Y.; Nomura, Y.; Paulatto, L.*, et al.*; Wannier90 as a Community Code: New Features and Applications. *J. Phys.: Condens. Matter* **2020,** *32*, 165902.
12. Singha, A.; Baltic, R.; Donati, F.; Wäckerlin, C.; Dreiser, J.; Persichetti, L.; Stepanow, S.; Gambardella, P.; Rusponi, S.; Brune, H.; 4f-Occupancy and Magnetism of Rare-Earth Atoms Adsorbed on Metal Substrates. *Phys. Rev. B* **2017,** *96*, 224418.
13. Donati, F.; Singha, A.; Stepanow, S.; Wäckerlin, C.; Dreiser, J.; Gambardella, P.; Rusponi, S.; Brune, H.; Magnetism of Ho and Er Atoms on Close-Packed Metal Surfaces. *Phys. Rev. Lett.* **2014,** *113*, 237201.
14. Donati, F.; Rusponi, S.; Stepanow, S.; Wäckerlin, C.; Singha, A.; Persichetti, L.; Baltic, R.; Diller, K.; Patthey, F.; Fernandes, E.; Dreiser, J.; Sljivancanin, Z.; Kummer, K.; Nistor, C.; Gambardella, P.; Brune, H.; Magnetic Remanence in Single Atoms. *Science* **2016,** *352*, 318-321.
15. Donati, F.; Rusponi, S.; Stepanow, S.; Persichetti, L.; Singha, A.; Juraschek, D. M.; Wäckerlin, C.; Baltic, R.; Pivetta, M.; Diller, K.; Nistor, C.; Dreiser, J.; Kummer, K.; Velez-Fort, E.; Spaldin, N. A.; Brune, H.; Gambardella, P.; Unconventional Spin Relaxation Involving Localized Vibrational Modes in Ho Single-Atom Magnets. *Phys. Rev. Lett.* **2020,** *124*, 077204.
16. Cowan, R. D., *The Theory of Atomic Structure and Spectra*. University of California Press: Berkeley, 1981.
17. Baltic, R.; Donati, F.; Singha, A.; Wäckerlin, C.; Dreiser, J.; Delley, B.; Pivetta, M.; Rusponi, S.; Brune, H.; Magnetic Properties of Single Rare-Earth Atoms on Graphene/Ir(111). *Phys. Rev. B* **2018,** *98*, 024412.
18. Goeller-Walrand, C.; Binnemans, K., Rationalization of Crystal-Field Parametrization. In *Handbook on the Physics and Chemistry of Rare Earths*, Gschneidner, K. A. J.; Eyring, L., Eds. Elsevier: Amsterdam, 1996; Vol. 23, pp 121-283.
19. Uldry, A.; Vernay, F.; Delley, B.; Systematic Computation of Crystal-Field Multiplets for X-Ray Core Spectroscopies. *Phys. Rev. B* **2012,** *85*, 125133.
20. Hummel, H.-U.; Fischer, E.; Fischer, T.; Joerg, P.; Pezzei, G.; Struktur Und Thermisches Verhalten Von Gadolinium(Iii)-Sulfat-Octahydrat $Gd_2(So_4)_3 \cdot 8\ H_2o$. *Z. Anorg. Allg. Chem.* **1993,** *619*, 805-810.
21. Dubrovin, V.; Popov, A. A.; Avdoshenko, S. M.; Valence Electrons in Lanthanide-Based Single-Atom Magnets: A Paradigm Shift in 4f-Magnetism Modeling and Design. *Inorg. Chem. Front.* **2021,** *8*, 2373-2384.